CELL THERAPY

Adoptive cell therapy with macrophage-drug conjugates facilitates cytotoxic drug transfer and immune activation in glioblastoma models

Miaomiao Sun[1]†, Maciej Bialasek[2,3]†, Maud Mayoux[4], Meng-Syuan Lin[5], Alicia Buck[1], Ilona Marszałek[2], Bartłomiej Taciak[2,3], Marcel Bühler[1], Małgorzata Górczak[2,3], Paulina Kucharzewska[2,3], Daria Kurpiel[2], Małgorzata Siemińska[2], Julia Nowakowska[2,3], Jan Brancewicz[2], Konrad Gabrusiewicz[2], Waldemar Lipiński[2], Sibylle Pfammatter[6], Steve Pascolo[7], Gregor Hutter[8,9], Lubomir Bodnar[10], Berend Snijder[11], Luca Regli[12], Michael Weller[1], Martin Baumgartner[5], Sonia Tugues[4,13], Tomasz P. Rygiel[2,14], Magdalena Krol[2,3]*, Tobias Weiss[1]*

The treatment of solid tumors faces substantial hurdles because of inadequate drug delivery and the immunosuppressive tumor microenvironment. To address these challenges, we developed a therapeutic platform using macrophages loaded with ferritin-drug conjugates, referred to as macrophage-drug conjugates (MDC), and applied it to glioblastoma, an immunologically cold solid tumor. MDC loaded with ferritin-conjugated monomethyl auristatin E enabled efficient, cell contact–dependent transfer of the payload by a mechanism involving transfer of iron-binding proteins, from either mouse or human macrophages preferentially into glioma cells. This targeted delivery and therapeutic efficacy was demonstrated across in vitro coculture systems, ex vivo assays using dissociated glioblastoma patient tumor samples, and in vivo using orthotopic glioblastoma mouse models, all while maintaining a favorable preclinical safety profile evidenced by minimal systemic toxicity and localized drug biodistribution. Beyond direct tumor cell killing leading to significant tumor regression and prolonged survival in these models, MDC therapy reprogrammed the immunosuppressive tumor microenvironment. Immune profiling by spectral flow cytometry revealed enhanced infiltration and activation of cytotoxic T lymphocytes and B lymphocytes while reducing immunosuppressive regulatory T cells. This culminated in a robust, durable, T cell–dependent antitumor immune response, the necessity of which was confirmed through studies in immunodeficient mouse models and by lymphocyte depletion, and which conferred protection against tumor rechallenge. The combined cytotoxic and immunomodulatory effects highlight the potential of MDC therapy as a promising strategy for glioblastoma treatment and support its further clinical development.

INTRODUCTION

Glioblastoma is the most common and most aggressive primary brain tumor in adults (*1*). Patients with this tumor have a poor prognosis, and there is an unmet medical need for more efficacious therapies. Persistent challenges include overcoming an immunosuppressive and tumor-promoting microenvironment and achieving safe and effective delivery of potent drugs to the tumor (*2*, *3*). The challenging tumor microenvironment is, in part, a consequence of the unique brain compartment. While growing in the brain, glioma cells recruit peripheral immune cells, particularly monocyte-derived macrophages, a phenomenon also observed in other solid tumors. These nonneoplastic cells constitute a substantial proportion of the cells within the tumor microenvironment, accounting for up to 40 to 50% (*4*, *5*). These macrophages constantly interact with glioma cells (*6*, *7*), which provides a strong rationale for macrophage-based therapies against challenging solid tumors such as glioblastoma. Current therapeutic strategies encompass the use of antibodies or small molecules to repolarize macrophages toward their antitumor functions, to inhibit their infiltration, or to deplete them (*8*). Concrete examples are the inhibition of C-C chemokine receptor type 2 (CCR2) or colony stimulating factor 1 receptor (*9*). However, the latter failed to demonstrate activity in a phase 2 clinical trial for patients with recurrent glioblastoma (*10*). Other approaches involve ex vivo engineering of macrophages to express chimeric antigen receptors or cytokines and then to reinject them back to the patients (*11*). These adoptive transfer strategies hold promise as an anticancer treatment because macrophages can be expanded to large numbers and modified in versatile ways. These developments have progressed to early clinical trials for various solid tumors (*12*).

Another challenge in glioblastoma, as in many solid tumors, is the efficient and safe delivery of highly cytotoxic drugs. This is of paramount importance because many drugs demonstrate potent

[1]Department of Neurology, Clinical Neuroscience Center, University Hospital Zurich and University of Zurich, 8091 Zurich, Switzerland. [2]Cellis AG, 8002 Zurich, Switzerland. [3]Center of Cellular Immunotherapies, Warsaw University of Life Sciences, 02-787 Warsaw, Poland. [4]Innate Lymphoid Cells and Cancer, Institute of Experimental Immunology, University of Zurich, 8057 Zurich, Switzerland. [5]Pediatric Molecular Neuro-Oncology Research, Division of Oncology, University Children's Hospital Zürich, 8008 Zürich, Switzerland. [6]Functional Genomics Center Zurich, ETH/University of Zurich, 8057 Zurich, Switzerland. [7]Department of Dermatology, University Hospital Zurich and University of Zurich, 8091 Zurich, Switzerland. [8]Brain Tumor Immunotherapy and Biology Laboratory, Department of Biomedicine, University of Basel, 4031 Basel, Switzerland. [9]Department of Neurosurgery, University Hospital Basel, 4031 Basel, Switzerland. [10]Faculty of Medical and Health Sciences, Siedlce University of Natural Sciences and Humanities, 08-110 Siedlce, Poland. [11]Institute of Molecular Systems Biology, Department of Biology, ETH Zurich, 8049 Zurich, Switzerland. [12]Department of Neurosurgery, Clinical Neuroscience Center, University Hospital Zurich and University of Zurich, 8091 Zurich, Switzerland. [13]Department of Immunology, Medical Faculty Mannheim, Mannheim Institute for Innate Immunosciences (MI3), 68167 Mannheim, Germany. [14]Laboratory of Immunology, Mossakowski Medical Research Institute, Polish Academy of Sciences, 02-106 Warsaw, Poland.
*Corresponding author. Email: m.krol@cellis.eu (M.K.); tobias.weiss@usz.ch (T.W.)
†These authors contributed equally to this work.

antitumor activity in vitro but their clinical application is often hindered by either extratumoral toxicity or poor distribution within the tumor (*13*). Current strategies to address these challenges encompass the use of nanocarriers or antibody-fusion proteins (*14*, *15*). One promising nanocarrier for targeted delivery is ferritin, which is biocompatible and biodegradable. Ferritin has a cage-like structure that enables the encapsulation or surface conjugation of payloads. However, in previously used administration strategies, its distribution within solid tumors relies on passive diffusion and remains limited (*16*).

In this study, we leveraged a recently described mechanism involving the transfer of iron-binding proteins (TRAIN) from macrophages to cancer cells to develop an adoptive cell therapy based on macrophage-drug conjugates (MDCs) (*17*) for glioblastoma treatment. We demonstrate the antitumor potential of this therapeutic approach against glioblastoma using advanced preclinical in vitro and in vivo models, achieving safe and efficient delivery of highly cytotoxic payloads into the cancer cells. MDCs after cancer cell killing phagocytosed cancer cell debris, activated immune response, and reprogrammed the immunosuppressive microenvironment into an immunologically active state, triggering a strong and durable antitumor immune response. We also explored combination strategies and the mechanisms governing the transfer of ferritin conjugates from macrophages to glioma cells. MDCs represent a versatile platform that demonstrate a dual mechanism of action, integrating targeted cytotoxicity with immune activation and offering a promising strategy for treating challenging solid tumors.

RESULTS

Macrophages transfer ferritin conjugates to glioma cells and MDCs exhibit potent antiglioma activity in vitro

To explore whether ferritin can be transferred from macrophages to glioma cells, we used two types of macrophages, murine bone marrow–derived macrophages (BMDMs) and human blood monocyte–derived macrophages (HMDMs). These macrophages were "loaded" with heavy chain ferritin (HFt), which was fluorescently labeled with Alexa Fluor 488 (AF488) for visualization by incubating macrophages in vitro with medium containing the HFt-AF488 protein. After internalization of HFt-AF488 into the macrophages, we cocultured these ferritin-loaded macrophages with the murine glioma cell lines SMA-560, SMA-497, GL-261, or CT-2A (Fig. 1A) or the human glioma cell lines ZH-305, ZH-161, LN-308, or LN-229 (Fig. 1B). Flow cytometry analysis showed a strong fluorescent HFt-AF488 signal in more than 90% of the glioma cells after 24 hours of coculture, indicating high efficiency of HFt transfer from macrophages to glioma cells in vitro. Confocal microscopy further confirmed this finding and demonstrated the presence of HFt-AF488 within glioma cells (Fig. 1, C and D). This transfer was conserved across species and seen using not only both murine and human primary macrophages but also human-induced pluripotent stem cell–derived macrophages as an alternative source for cell therapies (fig. S1, A to C). Time-lapse microscopy of the kinetics of the ferritin transfer from macrophages to glioma cells revealed that approximately 50% of glioma cells had taken up ferritin within 10 hours of coculture, and saturation in ferritin uptake was reached after 20 hours (fig. S1D).

Next, we harnessed the transfer of HFt from macrophages to cancer cells for therapeutic purposes. We conjugated ferritin by a valine-citrulline biodegradable linker with monomethyl auristatin E (vcMMAE), a highly toxic antimitotic agent frequently used as a payload for antibody-drug conjugates (ADCs) that has also been investigated against glioblastoma (*18*). This resulted in an HFt-vcMMAE complex named HFt-735 (fig. S1, E and F). We chose MMAE for its microtubule-disrupting mechanism, which complements DNA-alkylating agents (temozolomide and lomustine) and circumvents MGMT-mediated (O-6-methylguanine-DNA methyltransferase) DNA-repair resistance in glioblastoma. The conjugation was validated through ultraviolet-visible spectroscopy (UV-Vis), dynamic light scattering, and liquid chromatography–mass spectrometry (LC-MS). LC-MS analysis confirmed the purity of the HFt-735 conjugate, revealing that only 0.0016% of the total drug was unbound MMAE (fig. S1F). Loading HFt-735 into macrophages to form MDCs (MDC-735) yielded a concentration of approximately 148.98 ng of MMAE per 10^6 of human macrophages and 38.98 ng for BMDMs (fig. S1G). We also investigated the release of MMAE by cleavage of the valine-citrulline linker by the cancer cell–abundant protease, cathepsin B, after macrophage-mediated transfer of HFt-735 to tumor cells (fig. S1, H and I). Cathepsin B expression was required in glioma cells for cytotoxicity, confirming the dependence of the linker on this enzyme for MMAE release (fig. S1, H and I). Coculture of HFt-735–loaded murine (Fig. 1E) or human monocyte–derived macrophages (Fig. 1, F and G) with species-matched glioma cells reduced glioma cell viability in a time- and concentration-dependent manner. The glioma cells in these cultures exhibited disrupted microtubules (Fig. 1H) and the subsequent formation of multinucleated cells as a result of improper spindle formation and cytokinesis (fig. S1J), affirming the antimitotic drug effect of MMAE. To confirm conjugate integrity within macrophages, HFt was dually conjugated with AF488 for direct visualization of HFt and with vcMMAE. Confocal microscopy then validated the intracellular colocalization of the AF488 signal from HFt with MMAE (detected using an anti-MMAE antibody), indicating that the HFt-vcMMAE conjugate remained intact (fig. S1K). Macrophages loaded with HFt without the drug did not exhibit antitumor activity compared with those loaded with the therapeutically effective HFt-735 (fig. S1L).

Time-lapse microscopy revealed that the viability of HFt-735–loaded macrophages decreased at a slower rate than cancer cells (Fig. 1G). These data suggest a window of time for macrophages to deliver the toxic payload to cancer cells while avoiding long-term persistence. In addition to this cytotoxic effect, we also observed stronger phagocytic activity of MDC-735 compared with control macrophages (fig. S1, M to O). Time-lapse microscopy captured the dynamic process of phagocytosis of CT-2A-zsGreen glioma cell fragments and debris by murine MDC-735 over a 48-hour coculture period (movies S1 and S2), and imaging flow cytometry confirmed the internalization of CT-2A-zsGreen inside the macrophages (fig. S1N). Further in vitro studies revealed that MDC-735 coculture exhibited superior glioma cell killing, compared with free MMAE or MMAE conjugated to bovine serum albumin (BSA) (fig. S2, A and B). These results demonstrated that conjugation of MMAE and HFt and loading the complex to macrophages is essential for therapeutic efficacy.

Promising antiglioma activity of intratumorally administered MDCs in orthotopic syngeneic and xenograft glioma mouse models

To investigate the transfer of ferritin from macrophages to glioma cells and the therapeutic potential of MDCs in vivo, we used immunocompetent mice bearing orthotopic gliomas. We implanted fluorescently labeled GL-261-iRFP720 murine glioma cells into the

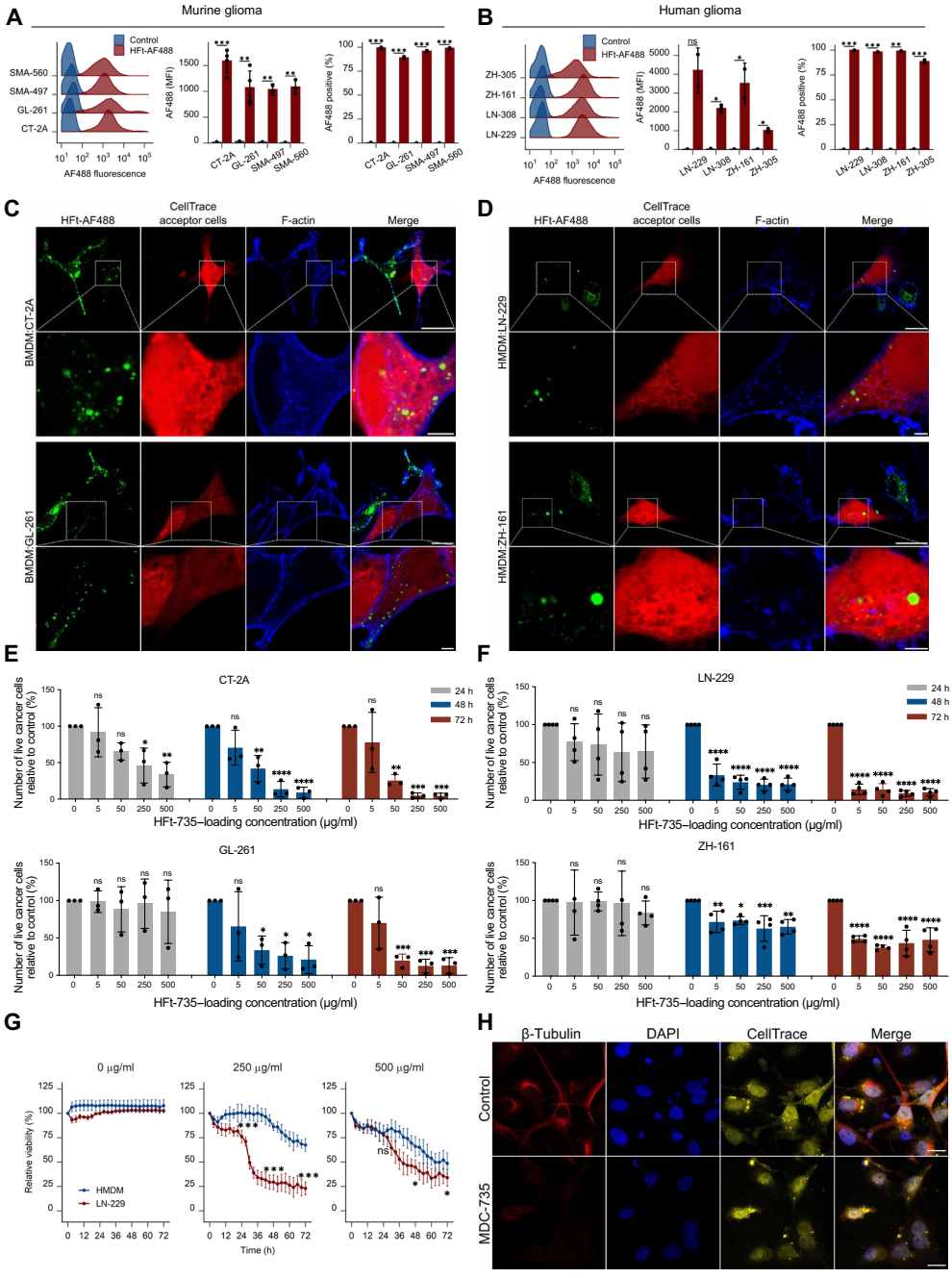

Fig. 1. Macrophages transfer HFt conjugates to glioma cells and MDC-735 has strong antiglioma activity in vitro. (**A** and **B**) Flow cytometry histograms and quantification of HFt-AF488 in murine (A) or human (B) glioma cells after coculture with HFt-AF488–loaded macrophages or unloaded control macrophages for 24 hours. Data presented as representative density plots (left) and bar plots of average geometric mean fluorescence intensity (geo-MFI) (middle), and the percentage of AF488-positive cells (right). Dots represent individual sample replicates. $n = 3$ independent replicates. (**C** and **D**) Representative confocal microscopy images illustrating HFt-AF488 in the murine glioma cell lines CT-2A (top) or GL-261 (bottom) (C) or HFt-AF488 fluorescence in human glioma cell lines LN-229 (top) and ZH-161 (bottom) (D) after 24 hours of HFt-AF488–loaded macrophage coculture. Dotted box indicates inset region magnified underneath. Scale bars, 20 μm; inset, 5 μm. (**E** and **F**) Quantification of flow cytometry analysis of glioma cell viability after 24-, 48-, or 72-hour coculture with macrophages loaded with varying concentrations of HFt-735 in murine (E) or human glioma cells (F). Viability is expressed as the number of live cancer cells relative to the control (0 μg/ml loading dose) condition. Dots represent individual sample replicates of $n = 3$ (E) or $n = 4$ (F). h, hours. (**G**) Quantification of time-lapse fluorescence microscopy analysis of viability changes in LN-229 human glioma cells (red) and HFt-735–loaded HMDMs (blue) over 72 hours of coculture, with images captured every 3 hours. $n = 3$ independent experiments based on two representative fields of view. (**H**) Representative confocal images demonstrating the microtubule-disrupting effects of MDC-735 on LN-229 glioma cells after 24 hours of coculture. Anti–β-tubulin staining (red); DAPI nuclear stain (blue); and CellTrace to visualize glioma cells (yellow). Scale bar, 10 μm. Data in (A), (B), (E), (F), and (G) are presented as means ± SD. Statistical analysis in (A) and (B) was performed using paired two-tailed Student's *t* test and in (E) to (G) was performed using one-way ANOVA with post hoc Tukey HSD test. ns ($P > 0.05$), not significant, $^*P < 0.05$, $^{**}P < 0.01$, $^{***}P < 0.001$.

brain, and after 7 and 11 days, we administered murine macrophages that were loaded ex vivo with HFt-AF790 or cell-free HFt-AF790, either intratumorally or intravenously (Fig. 2A and fig. S3, A to C). Ex vivo flow cytometry (fig. S3D) and microscopy (Fig. 2B) showed the presence of an HFt-AF790 signal specifically in the iRFP720-positive and CD45-negative glioma cells, confirming the in vivo transfer of ferritin from macrophages to glioma cells. In vivo imaging using fluorescence molecular tomography (FMT) revealed that the intratumoral administration of macrophages loaded with fluorescently labeled ferritin resulted in detection of the ferritin signal solely in the brain tumor area. Conversely, intravenous administration led to a ferritin signal in the liver and lung for both macrophage-HFt-AF790 and free HFt-AF790. However, in the tumor area, the signal was detected only with macrophage-HFt-AF790 and not with free HFt-AF790 (fig. S3, A to D), indicating that the macrophage-based approach is favorable for tumor targeting. However, intratumoral administration is the most efficient route to get a high effector cell number to the tumor site, making it the currently preferred administration route for cell therapies against glioblastoma (*19*, *20*).

Flow cytometry was used to check whether loading BMDMs with HFt-735 to generate MDC-735 might skew the cells toward an M2-like phenotype, which is typically associated with immunosuppression and tumor promotion. To address this, we compared the phenotype of MDC-735 to that of monocytes and empty BMDMs (M0 macrophages). There were no significant differences in surface marker expression between M0 macrophages and MDC-735 (fig. S3, E and F), suggesting that drug loading did not induce an M2 polarization. MDC-735 retained robust antitumor activity even in the presence of immunosuppressive, human M2-like macrophages (M2A and M2C), indicating its therapeutic potential within highly immunosuppressive tumor microenvironments (fig. S3, G and H).

To better understand the distribution and therapeutic impact of MDC-735, we conducted an experiment using an organotypic glioblastoma brain slice model (fig. S4A). This model demonstrated that MDC-735 cells were able to penetrate the tumor and deliver the 735 drug to the tumor cells more effectively compared with the administration of free components (a mixture of macrophages, HFt, and 735 drug) (Fig. 2C and fig. S4, B to D). Moreover, in the MDC-735–treated group, the tumor ex vivo was smaller than in the group treated with a mix of free macrophages, HFt, and 735 drug (fig. S4E). This result underscores the necessity of loading macrophages with the HFt-735 complex instead of treating macrophages with free HFt and free 735 drug.

Next, we assessed the therapeutic potential of MDC-735 in two orthotopic, immunocompetent murine glioma models, GL-261 and CT-2A (Fig. 2, D to F). Unloaded macrophages and free HFt-735 served as a control. Free MMAE has been reported to be lethal upon administration to mice (*21*) and therefore cannot be used as a free drug but can serve as a highly potent payload usually in a form of an ADC or a protein-drug conjugate (*22*). Although we also observed toxicity of the cell-free HFt-735 complex and no antitumor activity of the unloaded macrophages, the treatment with MDC-735 was well tolerated, reduced the tumor growth, and conferred a survival benefit compared with controls (Fig. 2, E and F). We explored this further in a therapeutic-window experiment in which CT-2A–bearing mice received one or two injections of MDC-735 at varying dose levels to determine the minimum effective and maximum tolerated doses balancing antitumor efficacy and safety (fig. S5A). Tumor size analysis showed a reduced tumor perimeter compared with the phosphate-buffered saline (PBS)–treated group (fig. S5, B and C). Administration of two injections of 2×10^6 MDC-735, the highest dose tested, led to improved survival outcomes as compared with a single treatment in CT-2A–bearing mice (fig. S5, D and E). Half of the group (three animals of six) achieved long-term survival. The magnetic resonance imaging (MRI) of three randomly selected animals from the PBS-treated and MDC-735–treated (two administrations of 2×10^6) groups on day 20 confirmed the presence of the tumor in all of the PBS-treated groups and in one animal of the MDC-735–treated group. In a group treated with one injection of 1×10^6 MDC-735, one animal of six achieved long-term survival, whereas in a group treated with two injections of 0.5×10^6 MDC-735, two animals of six achieved long-term survival (fig. S5, D and E). This experiment suggests that optimal macrophage dose is important for maximizing the therapeutic outcome.

In CT-2A model, we introduced additional controls. We investigated the antitumor activity of intratumorally administered macrophages loaded with free MMAE, and, additionally, we investigated the antitumor activity of intratumorally administered BSA-MMAE complex. None of these groups conferred a survival benefit as observed with MDC-735, confirming that macrophage loading of HFt-735 has the most promising antiglioma activity (fig. S5, F and G). MDC-735 also demonstrated a long-term antitumor effect, where five of six mice survived initial treatment of CT-2A gliomas (2×10^6 MDC-735), and of those, four (out of five) remained tumor-free after rechallenging 6 months later with glioma cells implanted in the contralateral hemisphere, without further therapy (Fig. 2G). This finding suggests the involvement of the immune system as a part of the response to MDC-735 treatment and induction of durable antitumor effect and induction of the immune resistance against glioma.

To investigate the translational potential of macrophage-ferritin drug conjugates for the treatment of glioblastoma, we examined the safety and efficacy of large-scale produced and cryopreserved human macrophages loaded with HFt-735 (MDC-735) in mice bearing orthotopic human ZH-161 glioma. We differentiated macrophages from monocytes isolated by leukapheresis from healthy donors using the CliniMACS Prodigy (Miltenyi) automated cell processing platform. These cells were then loaded with HFt-735 to create MDC-735 and cryopreserved until use. Flow cytometry demonstrated that the macrophage markers CD14, 25f9, and SR-A1 did not differ between control macrophages and MDC-735. However, MDC-735 expressed less of the immunosuppressive and phagocytosis inhibitory marker SIRPα compared with unloaded macrophages (fig. S3, E and F). We injected MDC-735 intratumorally into ZH-161-iRFP720 glioma–bearing mice on days 7 and 14 after tumor cell implantation. We monitored tumor growth by in vivo imaging using FMT (Fig. 2H). The treatment was well tolerated, reduced tumor growth, and conferred a survival benefit, with four of six mice achieving long-term survival (Fig. 2I and fig. S6, A and B). These data demonstrate the therapeutic activity and feasibility of MDC-735 as a cryopreserved, readily available treatment, highlighting its potential for development in clinical applications.

MDC-735 has a promising preclinical safety profile

To assess the safety of MDC-735, we first investigated the cytotoxicity against cancer cells or nonmalignant primary cells in cocultures in vitro. After 72 hours of coculture, MDC-735 preferentially reduced the viability of LN-229 glioma cells compared with nonmalignant primary astrocytes, primary hippocampal neurons, or primary

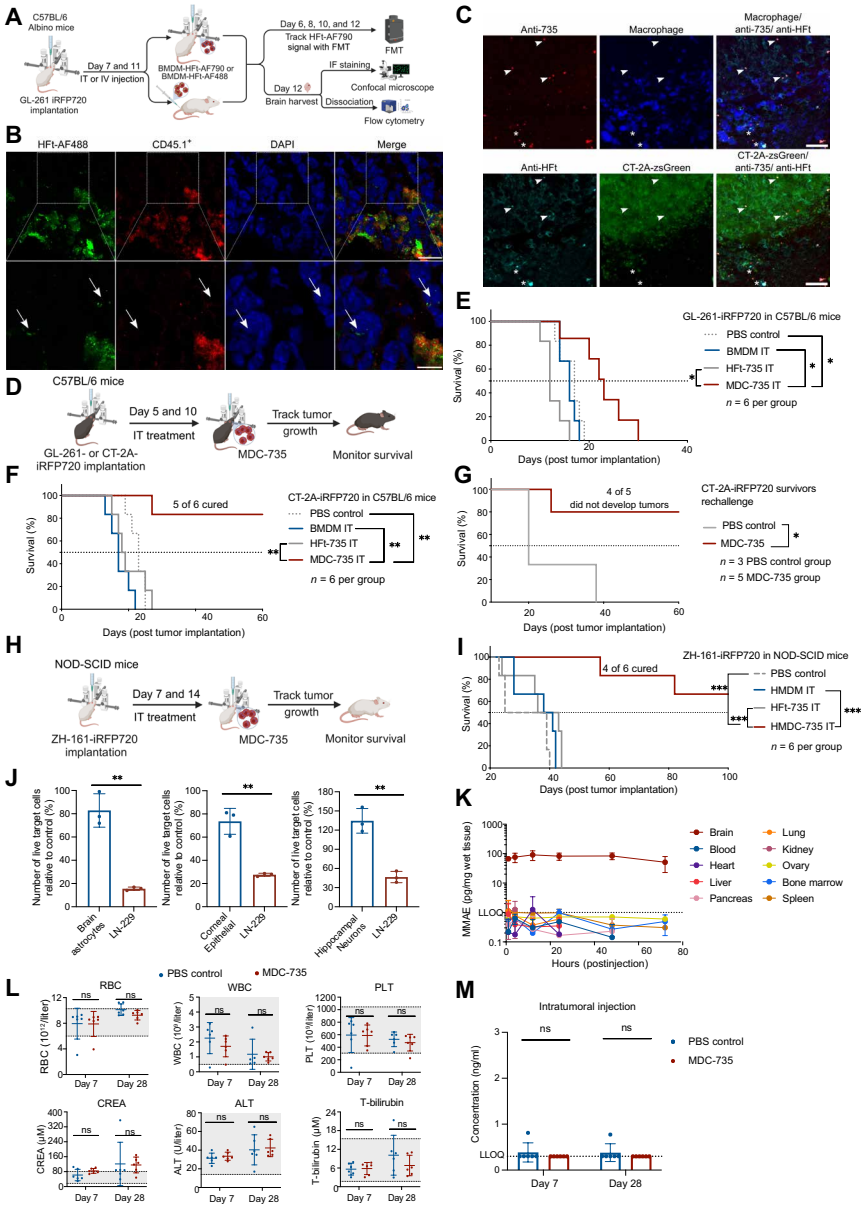

Fig. 2. Antiglioma activity and safety of intratumorally administered MDC-735 in orthotopic syngeneic and xenograft glioma mouse models. (**A**) Schematic of the experimental design illustrating the in vivo treatment schedule and analysis workflow for tracking fluorescent HFt conjugate–loaded macrophages in GL-261 tumor–bearing mice. IT, intratumoral; IV, intravenous. (**B**) Representative confocal microscopy images of brain sections from the tumor-bearing mice intratumorally treated with mouse BMDM loaded with HFt-AF488. Arrows identify HFt-AF488 that colocalizes with a non-CD45.1$^+$ cell. White dashed box indicates magnified area below. Scale bars, 20 μm; inset, 10 μm. (**C**) Representative confocal microscopy images showing a tumor cross section in an organotypic CT-2A-zsGreen glioblastoma brain slice model after injection of BMDM-HFt-735. Arrowheads indicate the presence of anti-735 antibody signal within the tumor area after 48 hours; asterisks indicate anti-MMAE signal within macrophages. Scale bar, 50 μm. (**D**) Schematic outline of the survival study of glioma-bearing mice that were treated IT on days 5 and 10 after tumor implantation with murine MDC-735. Negative controls include PBS, unloaded macrophages, and cell-free HFt-735 conjugate. (**E** and **F**) Kaplan-Meier survival curves for GL-261– (E) or CT-2A (F) glioma tumor–bearing mice receiving IT treatment with murine MDC-735 or controls. $n = 6$ mice per group. (**G**) Survival analysis of mice surviving initial CT-2A glioma implantation (F) and rechallenged 6 months later with CT-2A cells in the contralateral hemisphere. Statistical significance was determined by log-rank test. PBS, $n = 3$; MDC-735, $n = 5$. (**H**) Scheme of the experimental design using human ZH-161-iRFP720 glioma–bearing mice with human MDC-735. (**I**) Kaplan-Meier survival curves for ZH-161 glioma–bearing mice treated with IT-administered human MDC-735. Controls included PBS, empty HMDMs, and free HFt-735 conjugate. $n = 6$ mice per group. (**J**) Viability analysis of primary astrocytes, corneal epithelial cells, hippocampal neurons, and LN-229 glioma cells by flow cytometry after 72-hour coculture with MDC-735. Data are expressed as means ± SD relative to control. Dots represent individual sample replicates. $n = 3$ independent replicates. (**K**) Concentration of MMAE in tissues at multiple time points after MDC-735 injection into the mouse brain. $n = 3$ per time point. (**L** and **M**) Hematology and serum chemistry profiles (L) and anti-drug antibody (ADA) concentrations (M) in plasma of human glioma–bearing mice after IT MDC-735 or PBS treatment. Dots represent individual sample replicates. $n = 6$ mice per group. Gray area represents normal concentrations for each parameter. Survival data [(E), (F), (G), and (I)] were analyzed using the log-rank test. One-way ANOVA with Tukey HSD post hoc test was used for multiple group comparisons in (J), (L), and (M). For all panels, ns ($P > 0.05$), not significant, $^*P < 0.05$, $^{**}P < 0.01$, $^{***}P < 0.001$. Schematic illustrations in (A), (D), and (H) were created with BioRender.

human corneal epithelial cells (Fig. 2J), which are the cells known to be affected by MMAE-related toxicity in patients.

We assessed the safety profile in vivo by evaluating biodistribution, blood cell counts, and blood biochemistry measures. Biodistribution analysis of the MMAE payload in different organs of orthotopic glioma–bearing mice treated with intratumoral administration of MDC-735 demonstrated that MMAE was detectable only in the brain over eight time points up to 72 hours. In other tissues, its concentration was below the lower limit of quantification (Fig. 2K). Analysis of blood cell counts did not reveal any alterations in red blood cells, white blood cells, or platelets upon intratumoral MDC-735 treatment measured 7 or 28 days after injection. The concentration of the kidney function marker creatinine and liver function markers alanine aminotransferase and total bilirubin remained unchanged (Fig. 2L), as did other blood counts (table S1). To further confirm the safety of intratumoral MDC-735, we measured anti-MMAE drug antibodies (ADAs) in the blood 7 and 28 days after intratumoral MDC-735 administration. ADA concentrations were below the detection range (Fig. 2M), indicating no immune response against the therapeutic payload in the circulation. Similar results were obtained in healthy mice that did not carry gliomas but were intracranially injected with MDC-735, suggesting that there is no systemic toxicity of MDC-735 (table S1 and fig. S6, C and D). Furthermore, ex vivo histopathological evaluation of various mouse tissues showed that the injected macrophages ($CD68^+$ cells) were present only in the brain tumor region 7 days after intratumoral MDC-735 treatment. However, by day 28, macrophages were no longer detectable in any tissue (figs. S7 to S9), indicating their relatively short lifespan. No organ abnormalities or morphological signs of toxicity were observed in any organ.

MDC-735 changes the tumor microenvironment and promotes a T cell–dependent antitumor immune response

Results from the rechallenge study, demonstrating durable tumor resistance in mice treated with MDC-735, suggested an immunological component of the treatment. To investigate the immunological aspects of MDC-735, we first investigated soluble proinflammatory cytokines and the T cell activation marker CD69 in cocultures of human LN-229 glioma cells, human unstimulated T cells, and either unloaded human monocyte-derived macrophages or human MDC-735 in vitro. The highest concentrations of the proinflammatory cytokines interleukin-6 (IL-6) and tumor necrosis factor–α (TNF-α) were detected in triple cultures with MDC-735 (Fig. 3A). An elevated IL-6 concentration was also detected ex vivo in plasma from murine CT-2A glioma–bearing mice on day 12 post–tumor implantation, 2 days after the second intratumoral MDC-735 treatment (Fig. 3B). Flow cytometry analysis revealed an increase in the lymphocyte activation marker CD69 in human T cells cocultured with human MDC-735 and human glioma cells compared with controls (Fig. 3C). Coculture of LN-229 cells with free MMAE did not activate increased CD69 expression on T cells in vitro (Fig. 3C). This result demonstrates increased CD69 expression by treatment with MDC-735 over the free drug (MMAE) in activation of T cells (Fig. 3C).

Subsequently, we investigated the immunological effects of MDC-735 treatment on the tumor microenvironment in vivo in fully immunocompetent orthotopic glioma–bearing mice. CT-2A glioma–bearing mice were treated intratumorally with PBS, plain BMDMs, cell-free HFt-735, or MDC-735 on day 7 after tumor implantation, and tissue resident immune cells were subsequently analyzed on day 15 by ex vivo spectral flow cytometry of the tumor-bearing hemisphere, the tumor-draining lymph nodes (TDLNs), and non–tumor-draining lymph nodes (non-TDLNs). This enabled the quantitative detection of different immune cell subsets as demonstrated in the Uniform Manifold Approximation and Projection (Fig. 3D) based on typical lineage markers (Fig. 3E and fig. S10A) and the gating strategy (fig. S10, B and C). Compared with controls, CT-2A glioma–bearing mice treated intratumorally with MDC-735 had the highest numbers of tumor-infiltrating B cells, neutrophils, and CD4 and CD8 T cells (Fig. 3F). Furthermore, CD8 T cells from MDC-735–treated mice exhibited the lowest expression of the exhaustion markers TOX (thymocyte selection–associated high mobility group box), CD279, and TIM-3 (T cell immunoglobulin and mucin domain–containing protein-3) (Fig. 3G). Also, the frequency of TIM-3/PD1 double–positive CD8 T cells that have impaired cytotoxic activity (Fig. 3H) (*23*) was reduced upon MDC-735 treatment (Fig. 3I). Collectively, these results suggest that MDC-735 treatment converts the immunosuppressive glioma tumor microenvironment into an immunologically active one.

In TDLNs, MDC-735–treated glioma-bearing mice exhibited lower numbers of regulatory T (T_{reg}) cells (Fig. 3J) and the $PD1^+/CD39^+$ subset of T_{reg} cells that mediate a highly immunosuppressive environment (Fig. 3K), whereas these populations were not meaningfully changed in the non-TDLNs (fig. S10, D and E). These results suggest that MDC-735 also reduces immunosuppression in the TDLNs, thereby promoting an antitumor immune response.

Given the potential of macrophages in shaping the tumor microenvironment and their potential to become tumor-associated macrophages, we also investigated the persistence of and phenotype of the intratumorally administered $CD45.1^+$ macrophages, either loaded with HFt-735 or not, that could be distinguished from the endogenous immune cells based on the congenic marker system CD45.1/CD45.2 (fig. S10F). One week after treatment, we detected fewer MDC-735 within the tumor compared with plain BMDMs, suggesting that MDC-735 persists less (fig. S10G). Furthermore, we observed phenotypic differences between administered plain BMDMs and MDC-735. MDC-735 exhibited a more proinflammatory phenotype compared with plain BMDMs, as demonstrated by decreased expression of the immunosuppressive markers CD206, arginase, PD-L1, and TIM-3, and increased expression of MHC-II (fig. S10, H and I).

These results suggest that MDC-735 stimulates antitumor immunity, promotes T cell activation, and prevents T cell exhaustion. To functionally prove these observations and to validate that the immunological effects of MDC-735 are important for its antitumor effects, we used immunodeficient nonobese diabetic–severe combined immunodeficient (NOD-SCID) mice lacking functional T, B, and natural killer cells and $RAG1^{-/-}$ mice lacking functional B and T lymphocytes. The curative potential of MDC-735 in immunocompetent mice (four of seven long-term survivals and five of seven long-term survivals, respectively) was abrogated in both immunodeficient mouse strains (Fig. 3, L and M), underscoring the critical involvement of lymphocytes in mediating this response. Subsequent depletion experiments confirmed the relevance specifically of T cells. After CD4 and CD8 T cell depletion, which was validated by flow cytometry (fig. S10J), the survival benefit and curative potential of MDC-735 (three of seven long-term survivals) were abrogated (fig. S10K). These comprehensive analyses collectively highlight the multifaceted impact of MDC-735 on the tumor microenvironment and the antitumor immune response it induces, reinforcing its potential as a therapeutic strategy for immunologically cold glioblastoma.

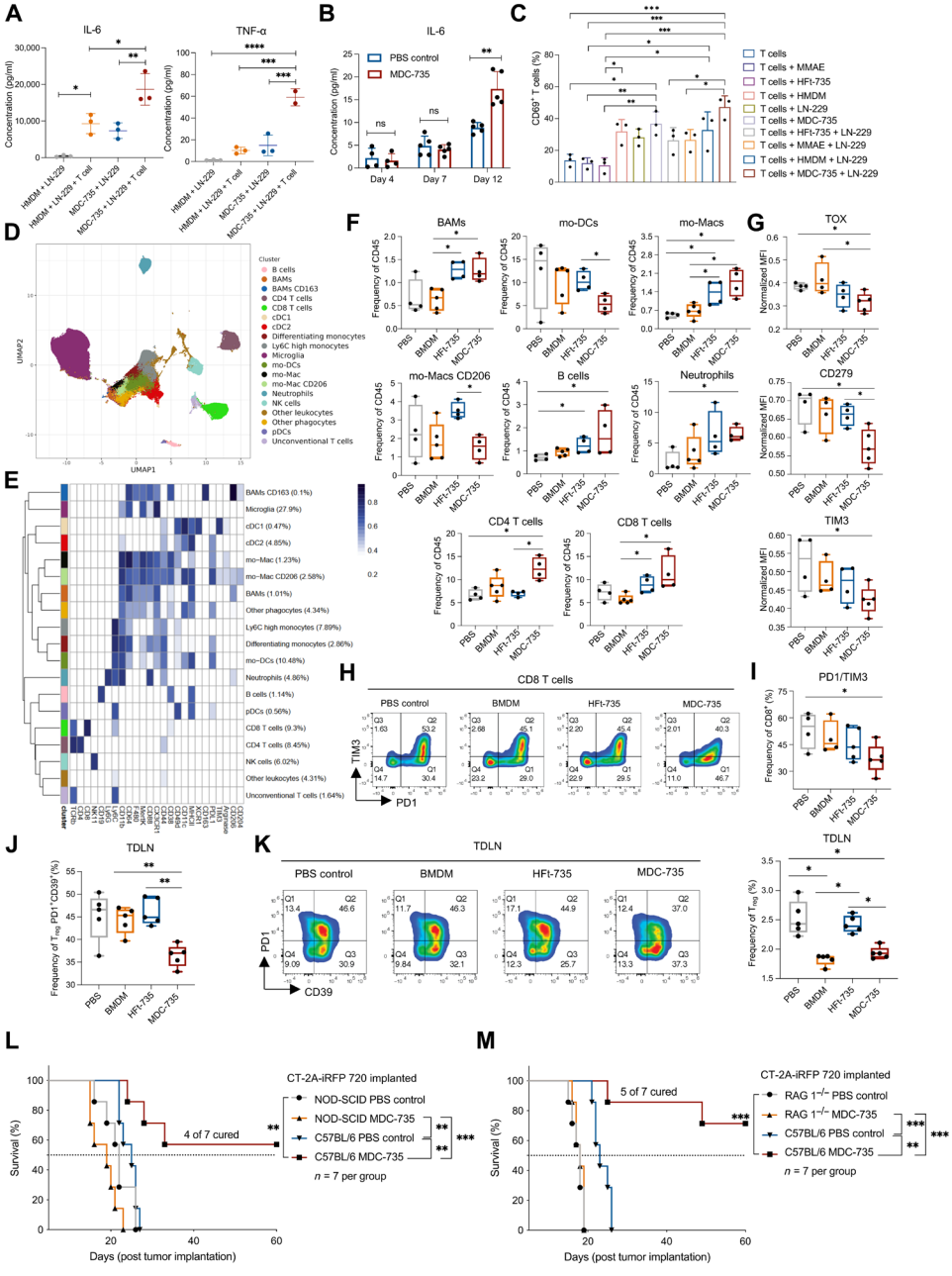

Fig. 3. MDCs change the tumor microenvironment and promote a T cell–dependent antitumor immune response. (**A**) Secreted IL-6 and TNF-α concentration in a 48-hour in vitro coculture of LN-229 glioma cells and T cells with MDC-735 or unloaded human MDMs as control. Data are presented as means ± SD; dots represent individual sample replicates. $n = 3$. (**B**) IL-6 concentration in peripheral blood plasma of CT-2A tumor–bearing C57BL/6 mice after IT MDC-735 or PBS treatment. Dots represent individual sample replicates. $n = 5$ per group. (**C**) CD69 expression on T cells, assessed by flow cytometry after 72-hour coculture with LN-229 glioma cells and MDC-735, compared with control groups. Data are presented as means ± SD; dots represent individual sample replicates. $n = 3$. (**D**) Uniform Manifold Approximation and Projection (UMAP) plot showing 12,000 cells per sample from each of the 17 mice, used for visualization of immune cell populations identified by spectral flow cytometry, in dissociated CT-2A tumor–bearing brain hemispheres from C57BL/6 mice treated with PBS, BMDM, HFt-735, or MDC-735. (**E**) Heatmap displaying key lineage marker expression across immune populations identified in (D). (**F**) Box plots comparing immune cell proportions across PBS (control), plain BMDMs, free HFt-735, or MDC-735 treatment. BAM, border-associated macrophages. Dots represent individual sample replicates. $n = 4$ or 5 per group. (**G**) $CD8^+$ T cell exhaustion marker expression across the treatment groups from (F). Dots represent individual sample replicates. $n = 4$ or 5 per group. (**H** and **I**) Density scatter plot of TIM-3 and PD1 (H) and quantification of the proportion of $CD8^+$ T cells expressing PD1 versus TIM-3. (I) Dots represent individual sample replicates. $n = 4$ or 5 per group. (**J**) Proportion of T_{reg} cells in the TDLNs across treatment groups. Dots represent individual sample replicates. $n = 4$ or 5 per group. (**K**) CD39 and PD1 expression on T_{reg} cells, along with the proportion of $CD39^+/PD1^+$ T_{reg} cells in the TDLNs. Dots represent individual sample replicates. $n = 4$ or 5 per group. (**L** and **M**) Kaplan-Meier curves of CT-2A glioma–bearing mice treated IT with MDC-735 or PBS in immunocompetent C57BL/6 mice (L) and immunodeficient NOD-SCID (M) or $RAG^{-/-}$ mice. $n = 7$ per group. Statistical analysis was performed using one-way ANOVA and Tukey HSD post hoc test (A), two-way ANOVA with Tukey post hoc test (C), unpaired two-tailed Student's *t* test (B), Wilcoxon unpaired test [(F), (G), (I), (J), and (K)], and log-rank test [(L) and (M)]. For all panels, ns ($P > 0.05$), not significant $^*P < 0.05$, $^{**}P < 0.01$, $^{***}P < 0.001$, $^{****}P < 0.0001$.

Local irradiation or chemokine receptor overexpression improves the therapeutic efficacy of intravenously administered macrophages carrying ferritin-drug conjugates

In line with the lower intratumoral accumulation of MDC-735 after systemic administration compared with intratumoral administration, the survival after intravenously administered MDC-735 was less extended than after intratumoral administration, and there was only one long-term surviving mouse in the CT-2A glioma model but none in the GL-261 glioma model (Fig. 4, A to C). However, because the intravenous administration route might be the only viable route in patients who are not eligible for intratumoral treatment, we investigated strategies to improve the migration of intravenously administered MDC-735 into orthotopically implanted gliomas to get more cells to the tumor site and to increase the antitumor effect of intravenously administered MDC-735. To achieve this, we used two strategies. First, we combined local low-dose tumor irradiation at days 6 and 10 after tumor implantation with intravenously administered MDC-735 at days 7, 9, 11, and 13 (Fig. 4D). Radiotherapy is a well-established glioma therapy, and low-dose irradiation has been shown to promote the migration of peripheral macrophages into tumors (*24*). In line with this, local pre-irradiation of the tumor site with 2 × 2 Gy facilitated the migration of fluorescently labeled macrophages into the tumor (Fig. 4E and fig. S11A), thereby enhancing the antitumor activity of systemically administered MDC-735 (Fig. 4, F to H, and fig. S11, B and C). In the fast-growing GL-261 model, two of six mice intravenously treated with MDC-735 achieved long-term survival.

As a second strategy, we conducted additional ex vivo engineering of macrophages and electroporated them with mRNA encoding for CCR2 (Fig. 4, I and J). CCR2 is a chemokine receptor that promotes macrophage migration in response to the chemokine CCL2 (*25*), which is overexpressed in glioma (*26*). After confirming that mRNA electroporation increased the cell-surface expression of CCR2 in primary murine macrophages and the cell line RAW264.7 as a control (Fig. 4K), we treated glioma-bearing mice with MDC-735 or MDC-735 additionally overexpressing CCR2. Macrophages overexpressing CCR2 exhibited improved migration activity toward the tumor (Fig. 4L and fig. S12A) and, once loaded with HFt-735, demonstrated stronger antiglioma effects (in the GL-261 model) with reduced tumor growth (fig. S12B) and prolonged survival. One mouse of six treated intravenously with MDC-735 achieved long-term survival (Fig. 4M).

The transfer of ferritin from macrophages to glioma cells depends on cell-cell contacts and involves cytoskeleton rearrangements and vesicle transfer

To elucidate the mechanisms underlying ferritin transfer from loaded macrophages to glioma cells, we investigated the requirement for cell-cell contact. For this, we used semipermeable membranes (Transwell) to physically separate macrophages loaded with fluorescent HFt from glioma cells during coculture, allowing molecule diffusion through the medium (Fig. 5A). This separation blocked the transfer, indicating a predominantly contact-dependent mechanism (Fig. 5B). High-resolution time-lapse microscopy confirmed direct cell-cell interactions between macrophages and glioma cells as well as the transfer of ferritin through these contact sites (fig. S13, A and B, and movies S3 and S4). To further characterize potential underlying molecular factors governing this contact-dependent process in glioma cells, we used affinity purification of biotinylated ferritin from macrophages or glioma cells separated after coculture followed by mass spectrometry to identify binding proteins to ferritin in macrophages or glioma cells. Through iterative experiments, we consistently identified 10 potential ferritin-binding proteins in macrophages or glioma cells after coculture (fig. S13C). Pathway enrichment analysis of these proteins revealed that the ferritin-binding proteins in macrophages were associated with processes such as cytoskeleton organization, regulation of protein localization to the cell periphery, and vesicle fusion (fig. S13D). In contrast, the proteins identified to bind to ferritin in glioma cells were associated only with cytoskeleton organization. The protein stabilin-1 (STAB1) was consistently detected in both macrophages and glioma cells. To support the role of this protein in the transfer of ferritin from macrophages to glioma cells, we used CRISPR-Cas9 to knock out the gene in the mouse macrophage cell line RAW264.7 and CT-2A glioma cell line. After confirming the expected truncation of the STAB1 gene in RAW264.7 and CT-2A cell lines (fig. S13E), we assessed the effect of the STAB1 knockout on the uptake of HFt-AF488 by macrophages and its subsequent transfer to glioma cells in coculture. STAB1 knockout in macrophages increased the uptake of HFt-AF488 in macrophages (fig. S13F) and also the transfer to glioma cells, whereas STAB1 knockout in CT-2A glioma cells had no effect (fig. S13G). These data supported the involvement of STAB1 in the transfer process from macrophages on a functional basis and suggest an inhibitory role for this protein.

To functionally validate whether the transfer occurs by the previously described, newly found TRAIN process (*27*), we used the vesicle marker CD63 and lipid membrane marker (PKH-67) to demonstrate the localization of HFt within intracellular vesicles in cancer cell (Fig. 5C). Furthermore, we used different inhibitors of intracellular vesicle formation and transport, like the phosphatidylinositol 3-kinase inhibitor wortmannin, the calpain inhibitor calpeptin, the neutral sphingomyelinase inhibitor GW4879, and the Rho kinase (ROCK) inhibitor Y-27632, which functionally validated that perturbations of intracellular vesicle formation or transport inhibit the transfer of ferritin from macrophages to glioma cells (Fig. 5D). Furthermore, we used imaging flow cytometry to validate a synapse-like structure forming between macrophages and cancer cells (Fig. 5, E and F). Quantitative imaging flow cytometry revealed F-actin accumulation at the macrophage-cancer cell interface (Fig. 5G), indicating an immune synapse-like structure. Inhibition of F-actin polymerization (using cytochalasin D and lantraculin B) reduced the transfer, confirming the involvement of actin dynamics (Fig. 5, H and I). Overall, these results confirmed involvement of TRAIN mechanism in HFt transfer from macrophages to glioma cells.

Macrophage-ferritin-drug conjugates have high translational potential with promising antitumor activity in complex glioblastoma patient samples

We explored the therapeutic activity of MDC-735 in samples from patients with complex glioblastoma directly obtained from surgery. We collected tumor samples from 20 patients with glioblastoma (table S4), dissociated them into single-cell suspension, and cocultured these complex tumor suspensions with ready-to-use frozen allogeneic primary human macrophages loaded with either fluorescently labeled HFt-AF647 (n = 10 patient samples) or HFt-735 (MDC-735) (n = 10 patient samples) (Fig. 6A). After 48 hours of coculture, we used an image-based single-cell functional profiling platform to characterize the effects of MDCs at the single-cell level

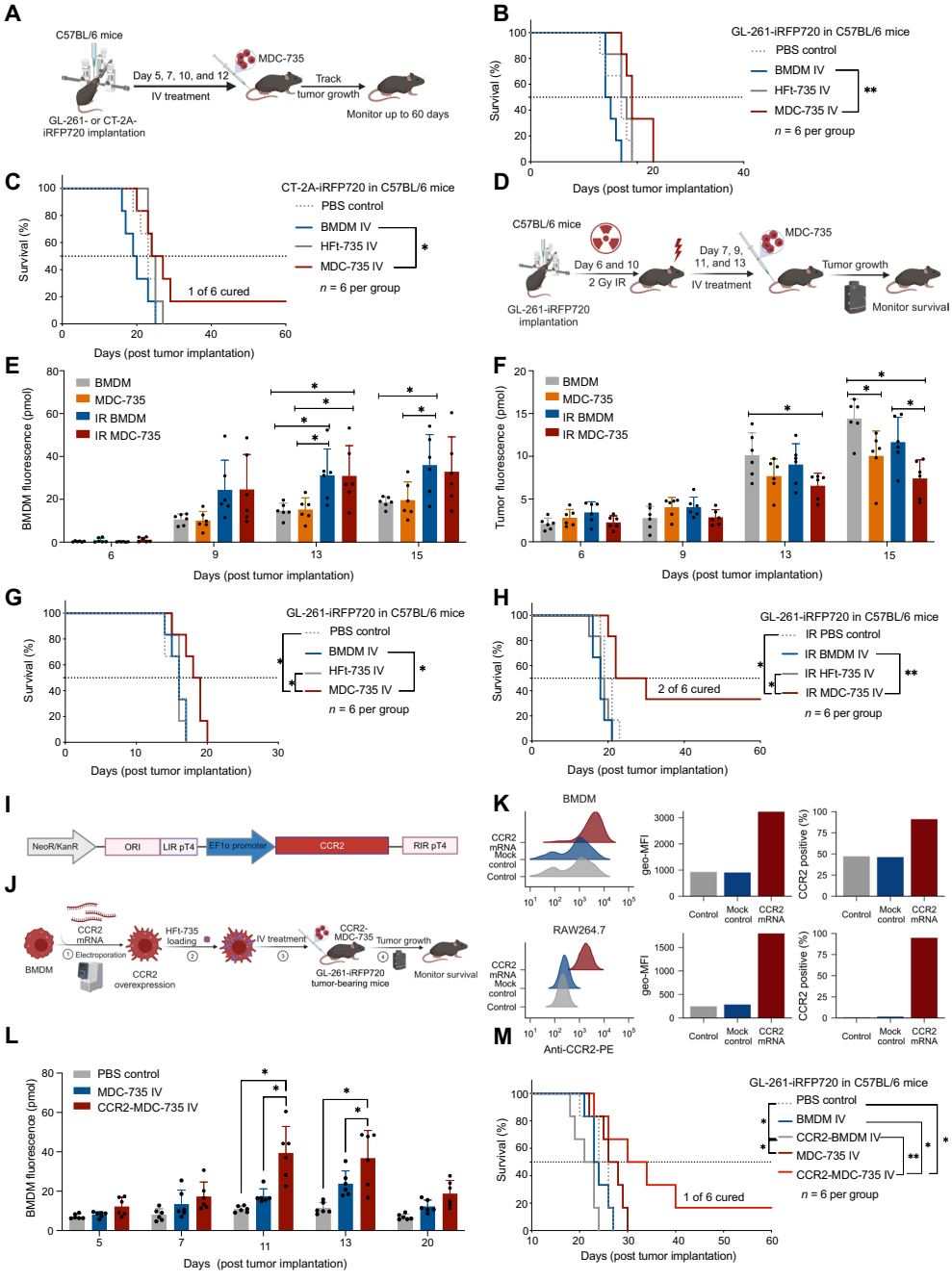

Fig. 4. Local irradiation or chemokine receptor overexpression improve the therapeutic efficacy of intravenously administered macrophages carrying ferritin-drug conjugates. (**A**) Schematic of the in vivo survival study design with IV administration of MDC-735 on days 5, 7, 10, and 12 after tumor cell implantation. (**B** and **C**) Kaplan-Meier survival curves for (B) GL-261 and (C) CT-2A glioma tumor–bearing mice treated IV with MDC-735 or controls. $n = 6$ per group. (**D**) Schematic of low-dose irradiation (IR) schedule (days 6 and 10) for combination therapy with IV-injected MDC-735 cells (days 7, 9, 11, 13). (**E**) FMT quantification of intratumoral BMDM or MDC-735 accumulation. FMT, fluorescence molecular tomography. (**F**) FMT quantification of GL-261-iRFP720 fluorescent tumor signal as a measurement of tumor burden. Data in (E) and (F) represent means ± SD; dots represent individual sample replicates. $n = 6$ mice per group. (**G** and **H**) Kaplan-Meier survival curves for GL-261-iRFP720 tumor–bearing mice treated with MDC-735, free HFt-735, unloaded BMDM, or PBS alone (G) or in combination with low-dose IR therapy (H). $n = 6$ per group. (**I**) Schematic diagram of the plasmid used for CCR2-encoding mRNA production. (**J**) Schematic of the in vivo survival study using macrophages electroporated with CCR2-encoding mRNA. (**K**) Flow cytometry histograms and analysis of RAW264.7 and BMDMs electroporated with CCR2 mRNA, mock-electroporated (Mock Control), or untreated (Control). (**L**) FMT quantification of fluorescence within a brain regions of interest (ROI) from MDC-735 and CCR2-overexpressing MDC-735 macrophages. Data represent means ± SD; dots represent individual sample replicates. $n = 6$ mice per group. (**M**) Kaplan-Meier survival curves for GL-261-iRFP720 tumor–bearing mice treated IV with CCR2-overexpressing MDC-735, MDC-735, empty BMDM (both CCR2-expressing and nonexpressing), or PBS. $n = 6$ mice per group. Statistical analysis was performed using one-way ANOVA with Tukey HSD post hoc test [(E), (F), and (L)] and log-rank test [(B), C), (G), (H), and (M)]. For all panels, ns ($P > 0.05$), not significant; $^*P < 0.05$ and $^{**}P < 0.01$. Schematic illustrations in (A), (D), and (J) were created with BioRender.

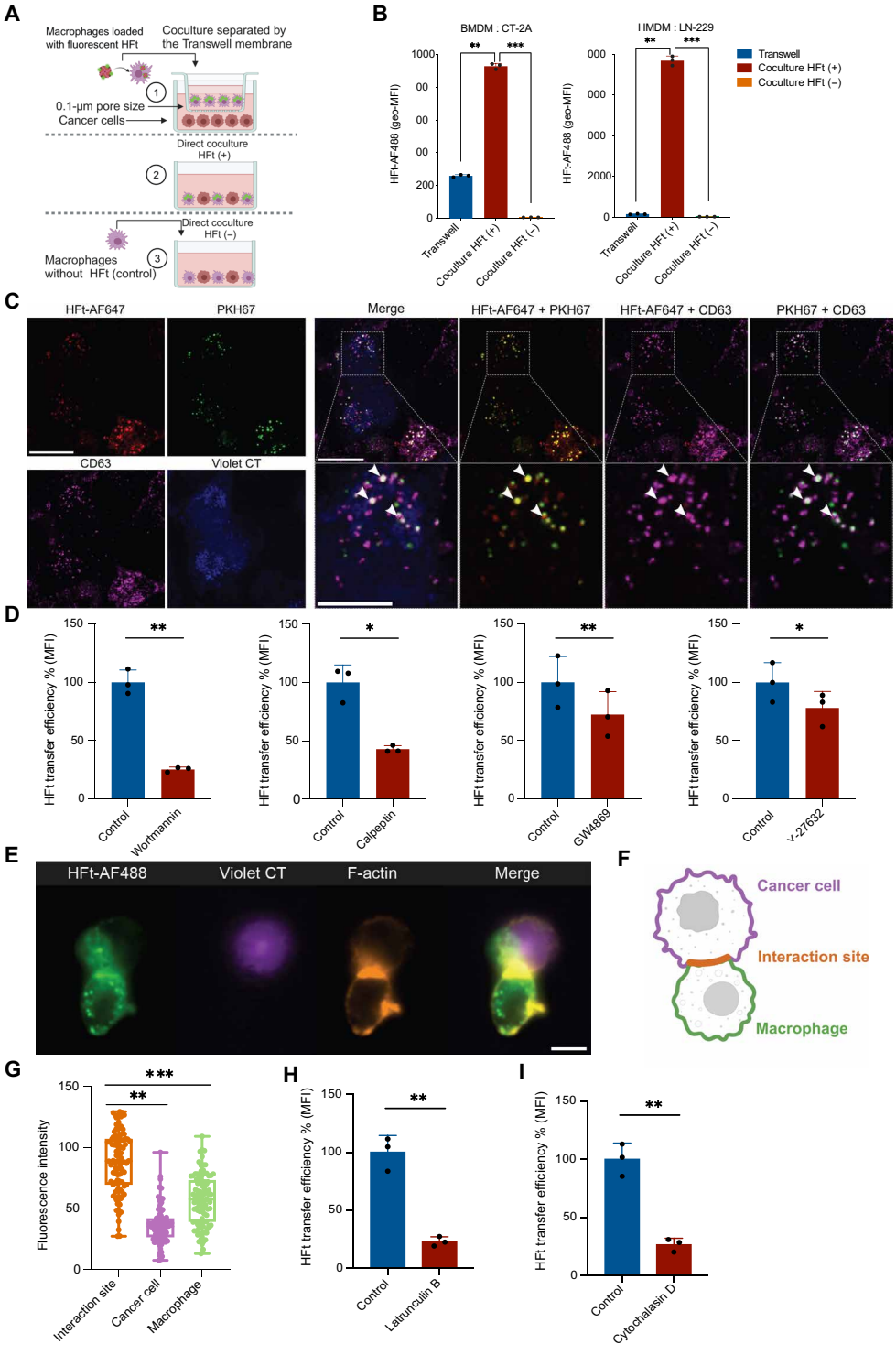

Fig. 5. The transfer of ferritin from macrophages to glioma cells depends on cell-cell contacts and involves cytoskeleton rearrangements and vesicle transfer. (**A**) Schematic representation of the in vitro coculture experiment setup. (**B**) Flow cytometry analysis of HFt-AF488 fluorescence in murine CT-2A (left) and human LN-229 glioma cells (right) after 24 hours of coculture with HFt-AF488–loaded macrophages. Data are presented as means ± SD; dots represent individual sample replicates. $n = 3$ independent replicates. (**C**) Representative confocal microscopy images showing HFt-AF488 fluorescence in LN-229 cancer cells (CellTrace Violet) after 24-hour coculture with PKH67-labeled HMDM-HFt-AF488 and anti-CD63 staining. Arrowheads highlight colocalization of AF488, PKH67, and CD63. Scale bar, 10 μm. (**D**) Flow cytometry analysis of relative AF488 MFI in glioma cancer cells after coculture with HFt-AF488–loaded macrophages, in the presence of inhibitors targeting vesicle formation and trafficking pathways. Data represent means ± SD; dots represent individual sample replicates. $n = 3$ independent replicates. (**E**) Representative imaging flow cytometry images of HMDM-HFt-AF488 and LN-229 cells (CellTrace Violet) stained with phalloidin-iFluor 555 for F-actin visualization. Scale bar, 7 μm. (**F**) Schematic representation of fluorescence quantification regions of interest (ROIs): macrophage ROI, cancer cell ROI, and cell-cell interaction site ROI. (**G**) HFt-AF488 fluorescence in each ROI defined in (F) based on imaging flow cytometry. Box and whiskers plots indicate the median and minimum and up to the maximum value. Data points represent fluorescence measurements from $n = 100$ representative images pooled from three independent replicates. (**H** and **I**) Relative AF488 MFI in cancer cells treated with latrunculin B (H) or cytochalasin D (I), inhibitors of actin polymerization, compared with vehicle control. Data represent means ± SD. Dots represent individual sample replicates. $n = 3$ independent replicates. Statistical analysis was performed using one-way ANOVA with Tukey's post hoc test [(B), (D), and (G)] or unpaired two-tailed Student's t test [(H) and (I)]. For all panels, ns ($P > 0.05$), not significant, $^*P < 0.05$, $^{**}P < 0.01$, $^{***}P < 0.001$. Schematic illustrations in (A) and (F) were created with BioRender.

(*28*). Despite interpatient heterogeneity, we observed a transfer of fluorescently labeled HFt from macrophages to glioma cells in 10 of 10 patient samples, with more glioma cells displaying a ferritin signal compared with nonmalignant cells from the tumor microenvironment in 8 of 10 patient cultures, suggesting a preferential transfer to cancerous cells (Fig. 6, B and C, and fig. S14, A and B).

In a separate set of 10 patient-derived dissociated tumor samples, we qualitatively assessed morphological changes in glioma cells and observed a more rounded cell shape, predominantly after MDC-735 treatment (Fig. 6D). To quantify phagocytic activity of macrophages, we performed a coculture of fluorescently labeled MDC-735 and Nestin$^+$-labeled glioma cells. Nestin was a key marker of cancer cells

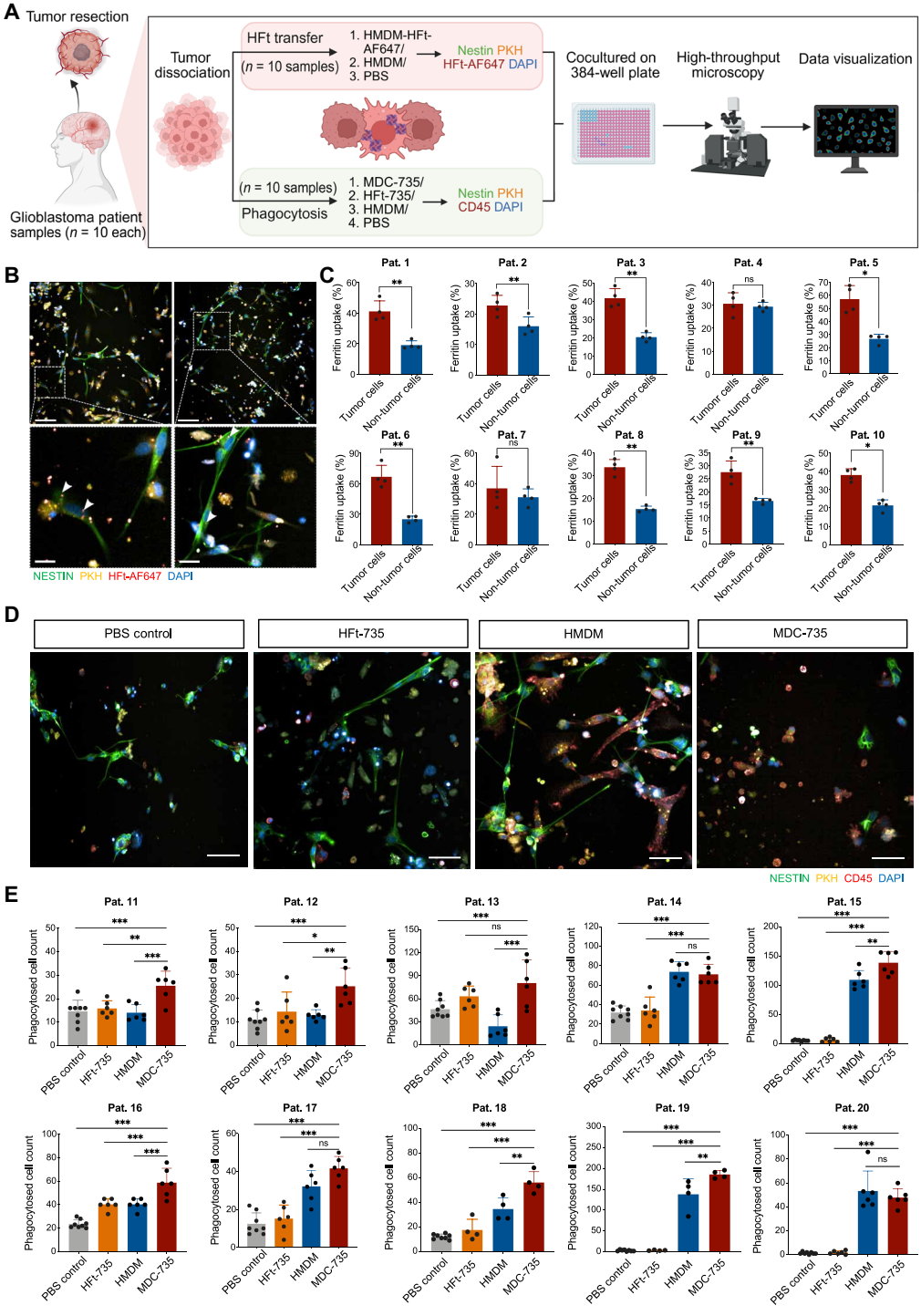

Fig. 6. MDCs have high translational potential in complex patient samples. (**A**) Schematic representation of the experimental setup. Dissociated human glioblastoma samples ($n = 20$ patient samples) were cocultured with HFt-AF647–loaded HMDMs ($n = 10$ patient samples, top) or with MDC-735 ($n = 10$ patient samples, bottom). (**B**) Representative immunofluorescence images showing HFt-AF647 transfer to Nestin$^+$ glioma cells. Arrowheads mark the HFt within Nestin$^+$ cells. White dashed box indicates location of magnified image below. Scale bar, 50 μm; inset, 10 μm. (**C**) Quantification of HFt-AF647 transfer into tumor versus nontumor cells in dissociated glioblastoma samples. Data represent means ± SD; dots represent technical replicates. $n = 4$ technical replicates per patient sample; $N = 10$ biological replicates, shown individually. Statistical analysis was performed using unpaired, two-tailed Student's t test. (**D**) Representative immunofluorescence images of Nestin$^+$ tumor cells cocultured with MDC-735 compared with control groups. Scale bar, 50 μm. (**E**) Comparison of the number of phagocytosed glioma cells (Nestin$^+$) in individual glioblastoma patient samples after exposure to MDC-735 or control treatments. Data represent means ± SD; dots represent technical replicates. $n = 4$ to 8 technical replicates per patient sample. Statistical analysis was performed using one-way ANOVA with Tukey's post hoc test. For all panels, ns ($P > 0.05$), not significant, $^*P < 0.05$, $^{**}P < 0.01$, $^{***}P < 0.001$. Schematic illustration in (A) created with BioRender.

and therefore was used to identify cancer cell debris within the macrophages. Analysis was done using an automatic image analysis platform to detect colocalization of fluorescent macrophage marker and Nestin. We observed substantial phagocytosis of glioma cells by allogenic macrophages, most notably in cocultures with HFt-735–loaded macrophages across all 10 patient samples. This suggests that MDC-735 enhances macrophage effector function compared with controls, supporting its potential therapeutic efficacy (Fig. 6E and fig. S14C).

DISCUSSION

Adoptive cell therapies, particularly ex vivo–engineered T cells, and ADCs with potent payloads yielded encouraging responses in extracranial malignancies (*29, 30*). However, recent studies in patients with glioblastoma, one of the most challenging tumors, have demonstrated only limited activity (*31*–*33*). Clinical trials of immune checkpoint blockade with nivolumab in recurrent glioblastoma showed no survival benefit over bevacizumab (*27*). Single-agent pembrolizumab in PD-L1–positive glioblastoma achieved a weak overall response rate (*27*). Barriers to effective treatment include immunosuppressive microenvironment, low mutation burden, sparse tumor-infiltrating lymphocytes, and poor drug delivery (*31*–*33*). Among nonmalignant cells, microglia and macrophages dominate the glioblastoma (GBM) microenvironment, making them logical targets for intervention or tools to be used against GBM (*34*, *35*). Prior macrophage-focused strategies—CSF-1R inhibition (to deplete or repolarize tumor-associated macrophages) and CCL2 blockade (to curb monocyte recruitment), ARG1/2, transforming growth factor–β, and hypoxia-inducible factor–1α blockade—showed limited clinical efficacy, underscoring the need for novel approaches (*10, 36*).

This study introduces the MDC "Trojan horse" strategy as an advanced therapeutic approach that combines targeted cytotoxicity with immune modulation by direct cell-to-cell transfer of ferritin-MMAE conjugates, avoiding nonspecific extracellular drug release (*37*–*39*). Our data supported that the efficacy of MDC-735 is driven by a newly found TRAIN mechanism involving the contact-dependent transfer of ferritin conjugates from macrophages to glioma cells, as demonstrated previously (*17*). Because direct cell-to-cell contact is required to occur, highly targeted delivery and safety are ensured.

MDC-735 produced significant survival benefits in both orthotopic xenografts and immunocompetent models without detectable toxicity. Free HFt + MMAE mixtures, as well as HFt-MMAE complex (without macrophages), failed to penetrate tumors or induce cytotoxicity, whereas HFt-MMAE–preloaded macrophages (MDC-735) achieved robust on-target cell death. Further results revealed bispecific mode of action of MDC-735. In addition to the direct antitumor effects, MDC-735 also demonstrated the ability to phagocytose glioma cell fragments and cellular debris. This underscores the critical role of macrophages not only in direct drug delivery but also in initiating a cascade of events leading to cancer cell killing and subsequent immune activation. HMDMs showed higher MMAE uptake than BMDMs, underpinning superior payload delivery. A two-dose intratumoral regimen further improved survival versus a single dose, emphasizing optimization of cell dose and schedule. In vivo experiments reinforced the translational potential of MDC-735, with intratumoral administration demonstrating robust tumor shrinkage and extended survival in orthotopic glioma models (CT-2A, GL261, and ZH-161). This approach drove robust and durable tumor regression and extended survival. In the CT-2A model, which exhibits mesenchymal differentiation and reduced interferon and antigen presentation pathways (characteristics akin to the aggressive mesenchymal human GBM subtype), five of six mice treated with MDC-735 survived for the entire 70-day study period. A curative effect in this model was confirmed by MRI in selected animals. To assess long-term tumor immunity, these long-term survivors were rechallenged 6 months later with implantation of CT-2A cells in the opposite hemisphere of the brain, and they resisted tumor growth, suggesting that MDC-735 not only eliminated tumors but also induced a durable, immune-mediated protective response. This suggests the potential for abscopal effects in multisite tumors, as evidenced by the long-term protection observed in rechallenged mice. Immune profiling revealed that MDC-735 treatment transformed the GBM microenvironment into an immunologically active one, marked by increased infiltration of cytotoxic T cells, B cells, reduced exhaustion markers, and lower frequencies of immunosuppressive regulatory T cells. These findings highlight the dual functionality of MDC-735 as both a cytotoxic agent and an immune modulator, making it uniquely suited for tackling immunologically cold tumors like GBM. Given the marked increase in granzyme-expressing $CD8^+$ T cells and reduction in PD-1 high exhausted phenotypes post–MDC-735, combining MDC-735 with checkpoint inhibitors (e.g., anti–PD-1) could potentiate T cell effector function.

Moreover, in samples derived from patients with complex GBM obtained directly from surgical procedures, which include both cancerous and nonmalignant cells from the tumor microenvironment, MDCs displayed a preference in transferring the ferritin conjugates to cancerous cells. Cytotoxicity testing revealed higher activity against glioma cells compared with noncancerous astrocytes, hippocampal neurons, and corneal epithelial cells, supporting the specificity of the MDC-735 approach in human primary tumor samples. The preclinical safety studies provide a compelling rationale for clinical translation. MDC-735 exhibited minimal systemic toxicity, with no detectable drug release into the circulation and no adverse effects on blood counts or organ function. It is a recurring problem with MMAE-containing ADCs: Such conjugates are highly potent but leak cytotoxin into the bloodstream (by cleavage-prone Val Cit linkers) or damage normal tissues that express the same antigen, leading to neutropenia, neuropathy, or bleeding (*40, 41*). In contrast, our biodistribution analysis confirmed that the MMAE payload remained localized within the tumor, further supporting the safety and specificity of this approach in mice.

Although intratumoral MDC-735 was superior, systemic delivery achieved better tumor homing after either focal preirradiation of tumor bed or macrophage CCR2 overexpression–enhanced CCR2-CCL2 axis migration. However, recent studies showed that intratumoral treatment in GBM may provide a clinical benefit for patients. In the phase 1 trial (NCT00805376), patients with recurrent, surgically accessible GBM were treated with a single intratumoral dose of an oncolytic virus, DNX-2401, by stereotactic biopsy needle or by implanted catheter. Objective tumor responses were observed in 72% of the needle-injected cohort, and median overall survival was 9.5 months in the needle group versus 13.0 months in the catheter group (*42*). Locoregional delivery of IL13Rα2-targeted CAR T cells by implantable reservoir–catheter systems has emerged as a promising strategy in GBM immunotherapy. Stable disease or better was achieved in 50% (29 of 58) of patients, with two partial responses, one complete response, and a second complete response after additional CAR T cycles off protocol. This outcome suggests that locoregional

cell therapy can elicit significant antitumor activity with manageable safety profiles (*19*).

The preclinical safety profile, combined with potent antitumor activity, makes MDC-735 a promising candidate for treating glioblastoma, providing an avenue for delivery of drugs like MMAE, which are typically limited by systemic toxicities (*43*). The platform's versatility enables the conjugation of various therapeutic agents to ferritin, as demonstrated by Taciak *et al.* (*17*), where this system was shown to be readily adapted for targeting other malignancies or delivering alternative therapeutic modalities, such as small-molecule inhibitors targeting specific oncogenic pathways, or even immunomodulatory agents like STING agonists, highlighting its adaptability for diverse oncological applications.

Although the results of this study are highly promising, there are a few limitations to note. The preclinical models used, including orthotopic glioma xenografts and immunocompetent mouse models, offer strong evidence of the therapeutic potential of MDC-735, although they do not fully replicate the human GBM tumor microenvironment. Similarly, even if ex vivo analyses conducted with patient-derived samples demonstrated targeted activity of MDC-735, this study does not capture the full heterogeneity of GBM and variability in therapeutic responses across different patient populations. Moreover, GBM remains one of the most treatment-resistant cancers, with profound barriers such as diffuse infiltration, rapid recurrence, and immune suppression, all of which will pose challenges even for novel approaches like MDC therapy. Future research should focus on evaluating the precise molecular mechanism of MDC-735–mediated immune activation to understand its role in T cell recruitment and reprogramming. Concurrently, it will be important to determine whether MDC-facilitated, MMAE-induced glioma cell death elicits enhanced immunogenic cell death signature. Such studies will deepen our mechanistic understanding and may reveal novel targets for synergistic therapeutic combinations.

An additional consideration is the clinical implementation of cell-based therapies in this context. MDC-735 uses allogeneic macrophages; their short-term lifespan and limited proliferation capacity may reduce the risk of long-term immune complications, supporting the feasibility of an off-the-shelf approach. Still, further validation in clinical settings is necessary to confirm consistent efficacy and durability of response.

In conclusion, MDCs demonstrate a functionally bispecific mechanism of action, integrating targeted cytotoxicity with immune activation. This dual-action profile is conceptually analogous to that of bispecific antibodies, which aim to bridge tumor cell recognition and immune cell engagement. This unique mechanism of action positions MDC-735 as a strong candidate for first-in-class therapy for GBM. Its favorable safety profile and ability to overcome key challenges in the tumor microenvironment further support its clinical potential. This innovative approach offers new hope not only for GBM but also for other solid tumors characterized by immunosuppressive and treatment-resistant niches.

MATERIALS AND METHODS

Study design

The primary aim of this study was to develop an adoptive transfer strategy for malignant brain tumors using macrophages loaded with iron-binding protein cages containing therapeutic drugs, enabling targeted delivery to cancer cells. This involved verifying the specificity and efficiency of payload transfer to glioma cells using in vitro co-culture systems, advanced microscopic visualization, and functional cytotoxicity assays. The second aim was to evaluate the translational potential of this approach using autologous and allogeneic macrophages loaded with the most efficient ferritin-drug conjugate for clinical application in patients with glioblastoma. We compared efficacy of the MDC-735 therapy in vivo and in patient-derived tumor ex vivo coculture studies. We used orthotopic glioma models, transplanting syngeneic, or xenograft glioma cells into mice to assess in vivo efficacy through survival studies, tumor burden monitoring, and analysis of antitumor immune responses (including immune cell profiling of tumor microenvironment and functional assays in immunodeficient models). A safety profile was generated by evaluating local and systemic drug concentrations, blood cell counts and biochemistry, and murine organ histology after treatment to support future clinical trial applications. Power analysis was performed to determine the appropriate sample size for animal experiments aiming to detect increase in median survival. The goal was to detect an anticipated 8-day increase in median survival (e.g., from an expected 17 days for control to 25 days for treated groups, with an estimated SD of 7 days), using a type I error rate (α) of 0.05 and 80% power ($1 - \beta$; $\beta = 0.20$). For the two in vivo studies using U-87 MG-luc cells, mice were randomized to treatment groups on the basis of bioluminescence signals after tumor establishment and before treatment initiation. In all other in vivo experiments described, mice were assigned to treatment groups cage by cage, and investigators assessing the outcomes in mice were not blinded to the treatment group. The number of replicates, group sizes, and statistical tests used in the analysis are indicated in the respective figure legends. Samples were excluded only if they did not meet technical requirements for downstream analyses (insufficient cell number or poor sample quality). This was the case for Fig. 3 (F, G, and I to K), Fig. 6E, and fig. S10 (D to E). No samples were removed on the basis of statistical outlier analysis.

Ferritin production

Cloning, expression, and purification process of the recombinant HFt (NCBI reference sequence: NP_002023.2) were provided by Genscript. The synthetic gene encoding HFt was designed to be optimal for *Escherichia coli* (*E. coli*) codon usage, cloned into a pET30a vector, and overexpressed in *E. coli* BL21 cells (plasmid sequence provided in data file S1). After inducing cell culture, the cells were lysed, and the supernatant was purified. Purification was based on the use of hydrophobic and ion exchange chromatography. The purity of the product was checked on SDS–polyacrylamide gel electrophoresis gel. The concentration of purified protein was calculated by measuring the UV-Vis using an extinction coefficient of 18,600 M^{-1} cm^{-1}.

Ferritin conjugation

To label HFt with fluorescent dyes such as AF488 and AF790, 10 mg of protein was diluted in 0.9 ml of PBS and buffered with 0.1 ml of 1 M sodium bicarbonate (pH 8.4) (Sigma-Aldrich). Alexa Fluor *N*-hydroxysuccinimide ester (succinimidyl ester) (Thermo Fisher Scientific) was dissolved in 50 μl of dimethyl sulfoxide (Sigma-Aldrich) and gently mixed with the HFt solution. The reaction tube was incubated for 1 hour at 25°C with continuous shaking at 500 rpm using a ThermoMixer (Eppendorf). The solution was then centrifuged at 10,000 rpm to remove any precipitate and subsequently washed using an Amicon Ultra-4 Centrifugal Filter Unit (Merck Millipore) with PBS until the ultrafiltrate was clear. The final concentration of labeled HFt was determined using UV-Vis spectrophotometry (NanoDrop 2000).

Conjugation of ferritin with drug 735 (MC-Val-Cit-PAB-MMAE, CAS no: 646502-53-6, MedChemExpress) was carried out with a

fivefold excess of drug over protein. Drug 735 was purchased from a commercial supplier with a declared purity of over 99.90% in the form of a powder and dissolved in a polar solvent before the reaction. The conjugation reaction buffer and the final formulation were based on an aqueous solution with a neutral pH. To assess conjugate purity, an LC-MS method was developed and optimized to separate MMAE from the HFt-735 conjugate. Calibration standards were prepared by serially diluting an MMAE standard (MedChemExpress) in 35% acetonitrile to establish a standard curve. Samples of the HFt-735 conjugate were injected directly without additional preparation or dilution. Chromatographic peaks corresponding to free MMAE from the resulting chromatograms were integrated, quantified, and compared against the standard curve to measure free MMAE concentrations. Using the drug-to-protein ratio, determined by LC-MS, and the protein concentration of the sample, as measured by UV-Vis spectroscopy, the total MMAE concentration in the conjugate was calculated. The ratio of free MMAE to the total MMAE (conjugated plus free) thus provides a measure of the purity of the HFt-735 conjugate preparation.

Animal experiments

Experiments were conducted in compliance with the guidelines set by the Swiss federal animal protection regulations and received approval from the regional veterinary authority (ZH079/2021). C57BL/6JRj (#SC-C57N-F), B6.129S7-Rag1^{tm1Mom}/J (RRID:MGI:2163461), and NOD.CB17-Prkdc^{scid} (#SM-NODS-F) male and female mice aged between 6 and 12 weeks were obtained from Janvier Labs and subsequently maintained in a pathogen-free environment at the Laboratory Animal Services Center of the University of Zurich. To determine the minimal number of animals per group, power analysis has been performed. The data from previous experiments with CT-2A model were used with the following anticipated parameters, expected mean survival of 17 days, with estimated variance of 7 days. Power of the test was 80% indicating minimal number of animals as six per group. For intracranial implantation, GL-261 (2×10^4), GL-261 iRFP720 (4×10^4), or CT-2A-iRFP720 (8×10^4) cells were stereotactically implanted into the right striata of C57BL/6 mice, whereas ZH-161-iRFP720 (8×10^4) cells were implanted into the right striata of NOD.CB17-Prkdc^{scid} mice on day 0. Daily observations were conducted for symptom emergence. Treatments were conducted either intravenously into tail vein (100 μl) or intratumorally (4 μl) using stereotactic implantations. MDC-735 was prepared directly before injection or prepared in advance and frozen. Differentiated macrophages were harvested, washed in PBS, resuspended in a 0.5 mg/ml solution of HFt-735 in serum-free macrophage medium, and incubated for 1 hour at 37°C in a 5% CO_2 atmosphere to allow HFt-735 uptake. After incubation, the macrophages were washed twice with PBS and resuspended at a concentration of 500×10^6 cells/ml for intratumoral injection and 50×10^6 cells/ml for intravenous injection. The schedules for these treatments are depicted in the schematics provided in the figures.

To assess potential tumor immunity in rechallenge study, the long-term survivors of CT-2A survival study as well as naïve mice as a control had tumor cells reimplanted into the opposite hemisphere of the brain. Survival of these mice were monitored without further treatment. T cell depletion experiments were performed using CD4 (clone GK1.5; #BE0003-1; BioXCell) and CD8 (clone 2.43; #BE0061; BioXCell) depletion antibodies. Depletion antibodies were intraperitoneally injected at 200 μg per mouse 1 day before tumor cell implantation and 100 μg every other 3 to 4 days. Cell depletion was confirmed by flow cytometry analysis of T cells isolated from blood samples collected from the tongue vein.

The isolation of tumor cells and tumor-infiltrating immune cells was conducted as described previously (*44*). Where described, local cranial irradiation with a low dose of 2 Gy was applied at days 6 and 10 after tumor implantation using a RS 2000 (serial # 3305) at 1 Gy/min. Mice bodies were covered with a lead plate, and only the tumor implantation sites were exposed to the fractioned radiation. Tumor growth was monitored using the FMT2500 (PerkinElmer) system. Where indicated, macrophages stained ex vivo with a 2 μM solution of CellBrite-NIR790 (Biotium) were also detected using the FMT2500. Image data were analyzed using the TrueQuant 3.1 software (PerkinElmer).

For therapeutic window experiment, MRI was performed with a 7T imager (Bruker BioSpin) at day 20 after tumor implantation. Coronal T2-weighted images were acquired by using ParaVision 360 (Bruker BioSpin). Tumor regions were identified manually by two independent raters, and the tumor perimeter was outlined and quantified using MIPAV (11.2.0).

Female athymic nude mice aged 5 to 7 weeks were used for the drug distribution study. The mice were bred in house by Axis Bio, all protocols used have been approved by the Axis Bioservices Animal Welfare and Ethical Review Committee (UK; project license PPL2885), and all procedures were carried out under the guidelines of the Animal Act 1986. Upon confirmation of tumor growth by U-87 MG-luc bioluminescence, mice were randomized into seven groups ($n = 3$): untreated and six groups of mice treated with MDC-735 (single dose of 2×10^6, intratumorally) with organ sampling point at 1, 4, 12, 24, and 72 hours after dose. The collected organs were weighted and frozen at −80°C.

Murine organotypic glioblastoma brain slice model

The coculture system of tumor spheroids and cerebellar slices was adapted from the protocol described (*44*). Briefly, cerebellar slices were prepared from postnatal day 9 (P9) to P11 wild-type C57BL/6JRj mice. Sagittal slices, 350 μm in thickness, were obtained using a vibratome (VT 1200S, Leica) and cultured on Millipore inserts (PICM 03050, Merck Millipore) for up to 10 days. The brain slice medium described in (*45*) was refreshed daily.

To generate tumor spheroids, CT-2A-zsGreen cells were seeded in low-attachment, round-bottom 96-well plates (4520, Corning) at a density of 5000 cells per well and cultured for 48 hours. For tumor-cerebellar coculture, a single tumor spheroid was carefully retrieved using a pipette and placed on top of a cerebellar slice. After 5 days of coculture, MDC-735 or mixture of BMDM, HFt, and MMAE components group were prepared and microinjected to tumor.

Microinjection was performed using a manipulator equipped with a 26-gauge needle (Small Hub RN Needle, 2 in, Point Style 5, 7784-07, Hamilton). The needle was positioned at the edge of the tumor spheroid, and 2 μl of the cell mixture for each experimental group was manually injected into the cerebellar slice. After microinjection, cerebellar slices were fixed with 4% paraformaldehyde (PFA) at 24 and 48 hours for subsequent immunofluorescence analysis.

For immunofluorescence analysis, the attached insert membrane and attached cerebellar slices were carefully trimmed and transferred into a 24-well plate for staining. The slices were permeabilized by incubation in trypsin-EDTA at 37°C in a humidified incubator for 5 min. Blocking was performed by incubating the slices in PBS containing 3% fetal bovine serum (FBS), 3% BSA, and 0.3% Triton

X-100 for 1 hour at room temperature. For primary antibody staining, anti-HFt (1:200) and anti-MMAE (1:25) antibodies were diluted in PBS containing 3% FBS and 3% BSA and incubated with the slices overnight at 4°C. Secondary antibodies were prepared in the same buffer (PBS containing 3% FBS and 3% BSA) and applied for 3 hours at room temperature. After thorough washing with PBS with 5% BSA, the slices were mounted using VECTASHIELD antifade mounting medium (H-1000-10, Vector Laboratories) for subsequent imaging. The image acquisition is performed using a Leica SP8 inversed confocal laser scanning microscope with 20× and 63× objectives.

Toxiciology study

Ninety Balb/c nude (RRID:IMSR_RJ:BALB-C-NUDE) mice (45 female, 45 male; 5 to 8 weeks old, 19 to 26 g) were sourced from Axis Bioservices and housed in individually ventilated cages with ad libitum access to a certified diet and sanitized water. Conditions were controlled at 20° to 24°C, 30 to 70% humidity, with a 12-hour light/dark cycle. The study's protocols received approval from the Axis Bioservices Animal Welfare and Ethical Review Committee, (UK; project license PPL2885) adhering to the Animal (Scientific Procedures) Act 1986 guidelines. Tumor cell implantation involved intracerebrally injecting U-87 MG-luc cells (1×10^5 in 5 μl Matrigel) into 54 mice using a 30-gauge needle. To confirm tumor growth, the animals were imaged at 1 and 2 weeks postimplantation. Mice with actively growing tumors confirmed were then randomly assigned to the treatment groups (PBS or 2.5×10^6 MDC-735 in 5 μl; intratumoral injection for tumor-bearing mice or intracerebral injection for control, healthy mice).

For blood analysis, at terminal sampling points (day 7 or day 28), blood was drawn from the tail vein of each subject for analysis. Subsequent evaluations included a complete blood count and a blood biochemistry profile. Blood samples were processed into plasma for ADA quantification. For enzyme-linked immunosorbent assay, 96-well plates were precoated with MMAE-BSA (Cell Mosaic, CM52113) at a concentration of 2 μg per well. Plasma samples from all subjects were then diluted 1:1000 in PBS and added to the wells. After washing, the wells were incubated with a horseradish peroxidase–labeled goat anti-mouse immunoglobulin G (IgG) antibody (BioLegend, 405306) and diluted to a final concentration of 0.4 μg/ml in blocking buffer (1:2000 dilution) to detect any mouse IgG.

For histopathology, upon termination, tissues including the brain (with tumor when applicable), femur, skin, intestines (small and large), heart, kidneys, liver, lungs, reproductive organs (ovary/testes), spleen, and stomach were harvested and embedded in paraffin blocks. Consecutive sections of 4 μm were prepared with a microtome; one set was stained with hematoxylin and eosin for general pathology evaluation, whereas the other was stained with an anti-CD68 antibody (Cell Signaling Technology, 26042).

Patient samples and image-based functional profiling of macrophages in complex glioblastoma patient samples

All samples involving humans were in accordance with the ethical guidelines outlined in the Declaration of Helsinki and upon approval from the Cantonal Ethics Committee (BASEC-Nr: 2019-01721). Patients with glioblastoma were included only after their consent. Glioblastoma patient samples were collected after surgery at the University Hospital of Zurich or Basel. Details of the glioblastoma patient cohort are provided in table S4. Single-cell suspensions were obtained as previously described (*4*). Tumor single-cell suspensions were mixed with healthy donor–derived HMDMs loaded with HFt-735 and labeled with PKH26 membrane dye in 2:1 ratio (1×10^4:0.5×10^4 cells) into clear-bottom, tissue-culture–treated, CellCarrier-384 Ultra Microplates (Perkin Elmer, #6057300). As control groups, patient single-cell suspensions were seeded alone, with empty PKH26-labeled HMDM or with free HFt-735 in the concentration equivalent to the amount in loaded HMDMs. After 48 hours of incubation at 37°C, 5% CO_2, cells were fixed with 4% PFA (Sigma-Aldrich), blocked with PBS containing 5% FBS, 0.1% Triton X-100, and 4′,6-diamidino-2-phenylindole (DAPI) (4 μg/ml, #422801, BioLegend) for 1 hour at room temperature and stained with AF488 anti-NESTIN (BioLegend, #656812, 1:500) and AF647 anti-CD45 (BioLegend, #368538, 1:300) overnight at 4°C. The 384-well plates were imaged using the Opera Phenix automated spinning-disk confocal microscope at 20× magnification (PerkinElmer, HH14000000). Cells were segmented on the basis of the DAPI channel using CellProfiler 2.2.0. Downstream image analysis was carried out with MATLAB R2021b. Marker-positive cells counts for each condition were determined on the basis of a linear threshold of the histograms of each channel. They were averaged per condition and compared against the control groups.

Statistical analysis

Data analysis was performed using R (R Core Team 2019) with R package "ggplot2" for data visualization (Wickham 2016) and GraphPad Prism 10. Normality of the data was assessed by the Shapiro-Wilk test. For comparisons between two groups, two-tailed unpaired or paired Student's *t* tests were used. When the normality assumption was not met, the nonparametric Wilcoxon test was applied instead. For comparisons involving more than two groups, one-way analysis of variance (ANOVA) followed by Tukey's post hoc test or two-way ANOVA followed by pairwise comparisons of estimated marginal means with Tukey correction was used, as stated in the figure legends. The survival data from in vivo studies were analyzed using the Kaplan-Meier method to estimate survival curves for each treatment group. Differences in survival rates between groups were evaluated using the log-rank (Mantel-Cox) test. To account for the increased risk of type I error due to multiple comparisons, the Bonferroni-Hochberg correction was applied to adjust *P* values. *P* value less than 0.05 was regarded as significant. Results are expressed as means ± SD unless otherwise stated. Box and whisker plots indicate the median (middle line), 25th and 75th percentiles (box) and minimum and maximum values (whiskers). All individual-level data are available in data file S2.

Supplementary Materials

The PDF file includes:

Materials and Methods
Figs. S1 to S14
Tables S1 to S4
Legends for movies S1 to S4
Legends for data files S1 and S2
References (*47*–*50*)

Other Supplementary Material for this manuscript includes the following:

Movies S1 to S4
Data files S1 and S2
MDAR Reproducibility Checklist

REFERENCES AND NOTES

1. Q. T. Ostrom, M. Price, C. Neff, G. Cioffi, K. A. Waite, C. Kruchko, J. S. Barnholtz-Sloan, CBTRUS statistical report: Primary brain and other central nervous system tumors diagnosed in the United States in 2015–2019. *Neuro Oncol.* **24**, v1–v95 (2022).

2. P. Y. Wen, M. Weller, E. Q. Lee, B. M. Alexander, J. S. Barnholtz-Sloan, F. P. Barthel, T. T. Batchelor, R. S. Bindra, S. M. Chang, E. A. Chiocca, T. F. Cloughesy, J. F. DeGroot, E. Galanis, M. R. Gilbert, M. E. Hegi, C. Horbinski, R. Y. Huang, A. B. Lassman, E. Le Rhun, M. Lim, M. P. Mehta, I. K. Mellinghoff, G. Minniti, D. Nathanson, M. Platten, M. Preusser, P. Roth, M. Sanson, D. Schiff, S. C. Short, M. J. B. Taphoorn, J. C. Tonn, J. Tsang, R. G. W. Verhaak, A. von Deimling, W. Wick, G. Zadeh, D. A. Reardon, K. D. Aldape, M. J. van den Bent, Glioblastoma in adults: A Society for Neuro-Oncology (SNO) and European Society of Neuro-Oncology (EANO) consensus review on current management and future directions. *Neuro Oncol.* **22**, 1073–1113 (2020).
3. M. Weller, M. van den Bent, M. Preusser, E. Le Rhun, J. C. Tonn, G. Minniti, M. Bendszus, C. Balana, O. Chinot, L. Dirven, P. French, M. E. Hegi, A. S. Jakola, M. Platten, P. Roth, R. Rudà, S. Short, M. Smits, M. J. B. Taphoorn, A. von Deimling, M. Westphal, R. Soffietti, G. Reifenberger, W. Wick, EANO guidelines on the diagnosis and treatment of diffuse gliomas of adulthood. *Nat. Rev. Clin. Oncol.* **18**, 170–186 (2021).
4. E. Friebel, K. Kapolou, S. Unger, N. G. Núñez, S. Utz, E. J. Rushing, L. Regli, M. Weller, M. Greter, S. Tugues, M. C. Neidert, B. Becher, Single-cell mapping of human brain cancer reveals tumor-specific instruction of tissue-invading leukocytes. *Cell* **181**, 1626–1642.e20 (2020).
5. F. Klemm, R. R. Maas, R. L. Bowman, M. Kornete, K. Soukup, S. Nassiri, J. P. Brouland, C. A. Iacobuzio-Donahue, C. Brennan, V. Tabar, P. H. Gutin, R. T. Daniel, M. E. Hegi, J. A. Joyce, Interrogation of the microenvironmental landscape in brain tumors reveals disease-specific alterations of immune cells. *Cell* **181**, 1643–1660.e17 (2020).
6. A. Buonfiglioli, D. Hambardzumyan, Macrophages and microglia: The cerberus of glioblastoma. *Acta Neuropathol. Commun.* **9**, 54 (2021).
7. D. Hambardzumyan, D. H. Gutmann, H. Kettenmann, The role of microglia and macrophages in glioma maintenance and progression. *Nat. Neurosci.* **19**, 20–27 (2016).
8. L. Cassetta, J. W. Pollard, Targeting macrophages: Therapeutic approaches in cancer. *Nat. Rev. Drug Discov.* **17**, 887–904 (2018).
9. B.-Z. Qian, J. Li, H. Zhang, T. Kitamura, J. Zhang, L. R. Campion, E. A. Kaiser, L. A. Snyder, J. W. Pollard, CCL2 recruits inflammatory monocytes to facilitate breast-tumour metastasis. *Nature* **475**, 222–225 (2011).
10. N. Butowski, H. Colman, J. F. De Groot, A. M. Omuro, L. Nayak, P. Y. Wen, T. F. Cloughesy, A. Marimuthu, S. Haidar, A. Perry, J. Huse, J. Phillips, B. L. West, K. B. Nolop, H. H. Hsu, K. L. Ligon, A. M. Molinaro, M. Prados, Orally administered colony stimulating factor 1 receptor inhibitor PLX3397 in recurrent glioblastoma: An Ivy Foundation Early Phase Clinical Trials Consortium phase II study. *Neuro Oncol.* **18**, 557–564 (2015).
11. A. Mantovani, P. Allavena, F. Marchesi, C. Garlanda, Macrophages as tools and targets in cancer therapy. *Nat. Rev. Drug Discov.* **21**, 799–820 (2022).
12. K. Pan, H. Farrukh, V. C. S. R. Chittepu, H. Xu, C.-X. Pan, Z. Zhu, CAR race to cancer immunotherapy: From CAR T, CAR NK to CAR macrophage therapy. *J. Exp. Clin. Cancer Res.* **41**, 119 (2022).
13. I. Noorani, J. de la Rosa, Breaking barriers for glioblastoma with a path to enhanced drug delivery. *Nat. Commun.* **14**, 5909 (2023).
14. T. Weiss, E. Puca, M. Silginer, T. Hemmerle, S. Pazahr, A. Bink, M. Weller, D. Neri, P. Roth, Immunocytokines are a promising immunotherapeutic approach against glioblastoma. *Sci. Transl. Med.* **12**, eabb2311 (2020).
15. T. Look, E. Puca, M. Bühler, D. Kirschenbaum, R. De Luca, R. Stucchi, D. Ravazza, C. D. Nitto, P. Roth, Y. Katzenelenbogen, A. Weiner, L. Rindlisbacher, B. Becher, I. Amit, M. Weller, D. Neri, T. Hemmerle, T. Weiss, Targeted delivery of tumor necrosis factor in combination with CCNU induces a T cell-dependent regression of glioblastoma. *Sci. Transl. Med.* **15**, eadf2281 (2023).
16. N. K. Lee, S. Cho, I.-S. Kim, Ferritin – a multifaceted protein scaffold for biotherapeutics. *Exp. Mol. Med.* **54**, 1652–1657 (2022).
17. B. Taciak, M. Bialasek, M. Kubiak, I. Marszalek, M. Gorczak, O. Osadchuk, D. Kurpiel, D. Strzemecki, K. Barwik, M. Skorzynski, J. Nowakowska, W. Lipiński, Ł. Kiraga, J. Brancewicz, R. Klopfleisch, Ł. Krzemiński, E. Gorka, A. Smolarska, I. Padzinska-Pruszynska, M. Siemińska, J. Guzek, J. Kutner, M. Kisiala, K. Wozniak, G. Parisi, R. Piacentini, L. Cassetta, L. M. Forrester, L. Bodnar, T. Weiss, A. Boffi, P. Kucharzewska, T. P. Rygiel, M. Krol, Harnessing macrophage-drug conjugates for allogeneic cell-based therapy of solid tumors via the TRAIN mechanism. *Nat. Commun.* **16**, 1327 (2025).
18. S. Parakh, J. Nicolazzo, A. M. Scott, H. K. Gan, Antibody drug conjugates in glioblastoma - Is there a future for them? *Front. Oncol.* **11**, 718590 (2021).
19. C. E. Brown, J. C. Hibbard, D. Alizadeh, M. S. Blanchard, H. M. Natri, D. Wang, J. R. Ostberg, B. Aguilar, J. R. Wagner, J. A. Paul, R. Starr, R. A. Wong, W. Chen, N. Shulkin, M. Aftabizadeh, A. Filippov, A. Chaudhry, J. A. Ressler, J. Kilpatrick, P. Myers-McNamara, M. Chen, L. D. Wang, R. C. Rockne, J. Georges, J. Portnow, M. E. Barish, M. D'Apuzzo, N. E. Banovich, S. J. Forman, B. Badie, Locoregional delivery of IL-13Rα2-targeting CAR-T cells in recurrent high-grade glioma: A phase 1 trial. *Nat. Med.* **30**, 1001–1012 (2024).
20. M. C. Burger, M. T. Forster, A. Romanski, F. Straßheimer, J. Macas, P. S. Zeiner, E. Steidl, S. Herkt, K. J. Weber, J. Schupp, J. H. Lun, M. I. Strecker, K. Wlotzka, P. Cakmak, C. Opitz, R. George, I. C. Mildenberger, P. Nowakowska, C. Zhang, J. Röder, E. Müller, K. Ihrig, K.-J. Langen, M. A. Rieger, E. Herrmann, H. Bonig, P. N. Harter, Y. Reiss, E. Hattingen, F. Rödel, K. H. Plate, T. Tonn, C. Senft, J. P. Steinbach, W. S. Wels, Intracranial injection of natural killer cells engineered with a HER2-targeted chimeric antigen receptor in patients with recurrent glioblastoma. *Neuro Oncol.* **25**, 2058–2071 (2023).
21. R. Qi, Y. Wang, P. M. Bruno, H. Xiao, Y. Yu, T. Li, S. Lauffer, W. Wei, Q. Chen, X. Kang, H. Song, X. Yang, X. Huang, A. Detappe, U. Matulonis, D. Pepin, M. T. Hemann, M. J. Birrer, P. P. Ghoroghchian, Nanoparticle conjugates of a highly potent toxin enhance safety and circumvent platinum resistance in ovarian cancer. *Nat. Commun.* **8**, 2166 (2017).
22. D. V. Hingorani, M. M. Allevato, M. F. Camargo, J. Lesperance, M. A. Quraishi, J. Aguilera, I. Franiak-Pietryga, D. J. Scanderbeg, Z. Wang, A. A. Molinolo, D. Alvarado, A. B. Sharabi, J. D. Bui, E. E. W. Cohen, S. R. Adams, J. Silvio Gutkind, S. J. Advani, Monomethyl auristatin antibody and peptide drug conjugates for trimodal cancer chemo-radio-immunotherapy. *Nat. Commun.* **13**, 3869 (2022).
23. M. Sawada, K. Goto, A. Morimoto-Okazawa, M. Haruna, K. Yamamoto, Y. Yamamoto, S. Nakagawa, K. Hiramatsu, S. Matsuzaki, E. Kobayashi, A. Kawashima, M. Hirata, K. Iwahori, T. Kimura, Y. Ueda, T. Kimura, H. Wada, PD-1$^+$ Tim3$^+$ tumor-infiltrating CD8 T cells sustain the potential for IFN-γ production, but lose cytotoxic activity in ovarian cancer. *Int. Immunol.* **32**, 397–405 (2020).
24. K. Zhai, Z. Huang, Q. Huang, W. Tao, X. Fang, A. Zhang, X. Li, G. R. Stark, T. A. Hamilton, S. Bao, Pharmacological inhibition of BACE1 suppresses glioblastoma growth by stimulating macrophage phagocytosis of tumor cells. *Nat. Cancer* **2**, 1136–1151 (2021).
25. T. M. Shroka, I. Kufareva, C. L. Salanga, T. M. Handel, The dual-function chemokine receptor CCR2 drives migration and chemokine scavenging through distinct mechanisms. *Sci. Signal.* **16**, eabo4314 (2023).
26. J. A. Flores-Toro, D. Luo, A. Gopinath, M. R. Sarkisian, J. J. Campbell, I. F. Charo, R. Singh, T. J. Schall, M. Datta, R. K. Jain, D. A. Mitchell, J. K. Harrison, CCR2 inhibition reduces tumor myeloid cells and unmasks a checkpoint inhibitor effect to slow progression of resistant murine gliomas. *Proc. Natl. Acad. Sci. U.S.A.* **117**, 1129–1138 (2020).
27. D. A. Reardon, A. A. Brandes, A. Omuro, P. Mulholland, M. Lim, A. Wick, J. Baehring, M. S. Ahluwalia, P. Roth, O. Bähr, S. Phuphanich, J. M. Sepulveda, P. De Souza, S. Sahebjam, M. Carleton, K. Tatsuoka, C. Taitt, R. Zwirtes, J. Sampson, M. Weller, Effect of nivolumab vs bevacizumab in patients with recurrent glioblastoma: The CheckMate 143 Phase 3 randomized clinical trial. *JAMA Oncol.* **6**, 1003–1010 (2020).
28. B. Snijder, G. I. Vladimer, N. Krall, K. Miura, A. S. Schmolke, C. Kornauth, O. L. de la Fuente, H. S. Choi, E. van der Kouwe, S. Gültekin, L. Kazianka, J. W. Bigenzahn, G. Hoermann, N. Prutsch, O. Merkel, A. Ringler, M. Sabler, G. Jeryczynski, M. E. Mayerhoefer, I. Simonitsch-Klupp, K. Ocko, F. Felberbauer, L. Müllauer, G. W. Prager, B. Korkmaz, L. Kenner, W. R. Sperr, R. Kralovics, H. Gisslinger, P. Valent, S. Kubicek, U. Jäger, P. B. Staber, G. Superti-Furga, Image-based ex-vivo drug screening for patients with aggressive haematological malignancies: Interim results from a single-arm, open-label, pilot study. *Lancet Haematol* **4**, e595–e606 (2017).
29. J. Z. Drago, S. Modi, S. Chandarlapaty, Unlocking the potential of antibody–drug conjugates for cancer therapy. *Nat. Rev. Clin. Oncol.* **18**, 327–344 (2021).
30. K. M. Cappell, J. N. Kochenderfer, Long-term outcomes following CAR T cell therapy: What we know so far. *Nat. Rev. Clin. Oncol.* **20**, 359–371 (2023).
31. N. Ahmed, V. Brawley, M. Hegde, K. Bielamowicz, M. Kalra, D. Landi, C. Robertson, T. L. Gray, O. Diouf, A. Wakefield, A. Ghazi, C. Gerken, Z. Yi, A. Ashoori, M. F. Wu, H. Liu, C. Rooney, G. Dotti, A. Gee, J. Su, Y. Kew, D. Baskin, Y. J. Zhang, P. New, B. Grilley, M. Stojakovic, J. Hicks, S. Z. Powell, M. K. Brenner, H. E. Heslop, R. Grossman, W. S. Wels, S. Gottschalk, HER2-specific chimeric antigen receptor-modified virus-specific T cells for progressive glioblastoma: A phase 1 dose-escalation trial. *JAMA Oncol.* **3**, 1094–1101 (2017).
32. D. M. O'Rourke, M. P. Nasrallah, A. Desai, J. J. Melenhorst, K. Mansfield, J. J. D. Morrissette, M. Martinez-Lage, S. Brem, E. Maloney, A. Shen, R. Isaacs, S. Mohan, G. Plesa, S. F. Lacey, J.-M. Navenot, Z. Zheng, B. L. Levine, H. Okada, C. H. June, J. L. Brogdon, M. V. Maus, A single dose of peripherally infused EGFRvIII-directed CAR T cells mediates antigen loss and induces adaptive resistance in patients with recurrent glioblastoma. *Sci. Transl. Med.* **9**, eaaa0984 (2017).
33. A. B. Lassman, S. L. Pugh, T. J. C. Wang, K. Aldape, H. K. Gan, M. Preusser, M. A. Vogelbaum, E. P. Sulman, M. Won, P. Zhang, G. Moazami, M. S. Macsai, M. R. Gilbert, E. E. Bain, V. Blot, P. J. Ansell, S. Samanta, M. G. Kundu, T. S. Armstrong, J. S. Wefel, C. Seidel, F. Y. de Vos, S. Hsu, A. F. Cardona, G. Lombardi, D. Bentsion, R. A. Peterson, C. Gedye, V. Bourg, A. Wick, W. J. Curran, M. P. Mehta, Depatuxizumab mafodotin in EGFR-amplified newly diagnosed glioblastoma: A phase III randomized clinical trial. *Neuro Oncol.* **25**, 339–350 (2023).
34. A. M. Miller, R. H. Shah, E. I. Pentsova, M. Pourmaleki, S. Briggs, N. Distefano, Y. Zheng, A. Skakodub, S. A. Mehta, C. Campos, W. Y. Hsieh, S. D. Selcuklu, L. Ling, F. Meng, X. Jing, A. Samoila, T. A. Bale, D. W. Y. Tsui, C. Grommes, A. Viale, M. M. Souweidane, V. Tabar, C. W. Brennan, A. S. Reiner, M. Rosenblum, K. S. Panageas, L. M. DeAngelis, R. J. Young, M. F. Berger, I. K. Mellinghoff, Tracking tumour evolution in glioma through liquid biopsies of cerebrospinal fluid. *Nature* **565**, 654–658 (2019).
35. F. Tang, Y. Wang, Y. Zeng, A. Xiao, A. Tong, J. Xu, Tumor-associated macrophage-related strategies for glioma immunotherapy. *NPJ Precis Oncol* **7**, 78 (2023).

36. U. Bogdahn, P. Hau, G. Stockhammer, N. K. Venkataramana, A. K. Mahapatra, A. Suri, A. Balasubramaniam, S. Nair, V. Oliushine, V. Parfenov, I. Poverennova, M. Zaaroor, P. Jachimczak, S. Ludwig, S. Schmaus, H. Heinrichs, K.-H. Schlingensiepen, the Trabedersen Glioma Study Group, Targeted therapy for high-grade glioma with the TGF-β2 inhibitor trabedersen: Results of a randomized and controlled phase IIb study. *Neuro Oncol.* **13**, 132–142 (2011).
37. J. Fu, D. Wang, D. Mei, H. Zhang, Z. Wang, B. He, W. Dai, H. Zhang, X. Wang, Q. Zhang, Macrophage mediated biomimetic delivery system for the treatment of lung metastasis of breast cancer. *J. Control. Release* **204**, 11–19 (2015).
38. V. D. Nguyen, H.-K. Min, H. Y. Kim, J. Han, Y. H. Choi, C.-S. Kim, J.-O. Park, E. Choi, Primary macrophage-based microrobots: An effective tumor therapy in vivo by dual-targeting function and near-infrared-triggered drug release. *ACS Nano* **15**, 8492–8506 (2021).
39. Y. Wang, L. Zhang, Y. Liu, L. Tang, J. He, X. Sun, M. H. Younis, D. Cui, H. Xiao, D. Gao, X.-Y. Kong, W. Cai, J. Song, Engineering CpG-ASO-Pt-loaded macrophages (CAP@M) for synergistic chemo-/gene-/immuno-therapy. *Adv. Healthc. Mater.* **11**, e2201178 (2022).
40. M. Mortaja, S. R. Adams, R. R. McKay, J. S. Gutkind, S. J. Advani, Spatially precise chemo-radio-immunotherapy by antibody drug conjugate directed tumor radiosensitization to potentiate immunotherapies. *NPJ Precis. Oncol.* **9**, 97 (2025).
41. T. D. Nguyen, B. M. Bordeau, J. P. Balthasar, Mechanisms of ADC toxicity and strategies to increase ADC tolerability. *Cancer* **15**, 713 (2023).
42. F. F. Lang, C. Conrad, C. Gomez-Manzano, W. K. A. Yung, R. Sawaya, J. S. Weinberg, S. S. Prabhu, G. Rao, G. N. Fuller, K. D. Aldape, J. Gumin, L. M. Vence, I. Wistuba, J. Rodriguez-Canales, P. A. Villalobos, C. M. F. Dirven, S. Tejada, R. D. Valle, M. M. Alonso, B. Ewald, J. J. Peterkin, F. Tufaro, J. Fueyo, Phase I study of DNX-2401 (Delta-24-RGD) oncolytic adenovirus: Replication and immunotherapeutic effects in recurrent malignant glioma. *J. Clin. Oncol.* **36**, 1419–1427 (2018).
43. R. Parrozzani, G. Lombardi, E. Midena, D. Londei, M. Padovan, G. Marchione, M. Caccese, G. Midena, V. Zagonel, L. Frizziero, Ocular side effects of EGFR-inhibitor ABT-414 in recurrent glioblastoma: A long-term safety study. *Front. Oncol.* **10**, 593461 (2020).
44. A. Neve, K. Santhana Kumar, D. Tripolitsioti, M. A. Grotzer, M. Baumgartner, Investigation of brain tissue infiltration by medulloblastoma cells in an *ex vivo* model. *Sci. Rep.* **7**, 5297 (2017).
45. J. Falsig, A. Aguzzi, The prion organotypic slice culture assay—POSCA. *Nat. Protoc.* **3**, 555–562 (2008).
46. Y. Perez-Riverol, C. Bandla, D. J. Kundu, S. Kamatchinathan, J. Bai, S. Hewapathirana, N. S. John, A. Prakash, M. Walzer, S. Wang, J. A. Vizcaíno, The PRIDE database at 20 years: 2025 update. *Nucleic Acids Res.* **53**, 543–553 (2025).
47. T. Weiss, H. Schneider, M. Silginer, A. Steinle, M. Pruschy, B. Polić, M. Weller, P. Roth, NKG2D-dependent antitumor effects of chemotherapy and radiotherapy against glioblastoma. *Clin. Cancer Res.* **24**, 882–895 (2018).
48. J. Weischenfeldt, B. Porse, Bone marrow-derived macrophages (BMM): Isolation and applications. *Cold Spring Harb. Protoc.* **2008**, pdb.prot5080 (2008).
49. G. G. Hesketh, J.-Y. Youn, P. Samavarchi-Tehrani, B. Raught, A.-C. Gingras, Parallel exploration of interaction space by BioID and affinity purification coupled to mass spectrometry. *Methods Mol. Biol.* **1550**, 115–136 (2017).
50. M. Tusup, L. E. French, M. De Matos, D. Gatfield, T. Kündig, S. Pascolo, Design of *in vitro* transcribed mRNA vectors for research and therapy. *Chimia (Aarau)* **73**, 391–394 (2019).

Acknowledgments: We would like to thank the Center for Microscopy and Image Analysis and the Cytometry Core Facility at University of Zurich and contractors from Core Facility for Crystallography and Biophysics, University of Warsaw (CFCB UW) for HFt purification. Proteomics analyses were performed with the support of the Functional Genomics Center Zurich (FGCZ) of University of Zurich and ETH Zurich. We would like to thank M. Sobczak from the Department of Botany, Institute of Biology, Warsaw University of Life Sciences for granting access to confocal microscope. Experimental schemes were created in BioRender. Weller, M. (2025): Fig. 2A (https://BioRender.com/u70x820), Fig. 2D (https://BioRender.com/m89l806), Fig. 2H (https://BioRender.com/w38j877), Fig. 4A (https://BioRender.com/c43g896), Fig. 4D (https://BioRender.com/n00r003), Fig. 4I (https://BioRender.com/u81t983), Fig. 4J (https://BioRender.com/p21m336), Fig. 5A (https://BioRender.com/a06l592), Fig. 5F (https://BioRender.com/k08t685), Fig. 6A (https://BioRender.com/a10f447), fig. S4A (https://BioRender.com/x07t185), fig. S5A (https://BioRender.com/i88e374), and. fig. S5F (https://BioRender.com/tmlcg6f). **Funding:** This research is funded by Cellis AG, National Center for Research and Development (NCBR, Poland), project no. POIR.01.01.01-00-0362/20 entitled "Innovative therapy for glioblastoma treatment" (to M.K.) and European Research Council, project AGAINST no. 101113272 (to M.K.). T.W. received support from Promedica Foundation (solely to T.W.), Sophien Foundation (to T.W. and M.W), Baasch-Medicus Foundation (solely to T.W.), the Helmut Horten Foundation (to T.W.), the Swiss Bridge Award SB-17-2024 (to T.W.) and the Swiss Cancer League (KFS-5763-02-2023, to T.W.). **Author contributions:** M. Sun, M. Bialasek, M.K., and T.W. designed and performed in vitro and in vivo experiments, analyzed the data, and wrote the manuscript. M.M. performed immunological ex vivo analysis. M.-S.L. performed organotypic glioblastoma brain slice imaging. A.B. performed the patient ex vivo profiling. I.M., B.T., M.G., P.K., D.K., W.L., M. Siemińska, J.N., J.B., and K.G. performed in vitro experiments and produced the ferritin conjugates. M. Bühler analyzed the AP-MS data. S. Pfammatter helped AP-MS acquisition. M. Bialasek, L.B., B.S., M.W., M. Baumgartner, S.T., S. Pascolo, L.R., T.P.R., and M.K. edited the manuscript. S. Pascolo generated the mRNA, and G.H. acquired glioblastoma tissue and edited the manuscript. **Competing interests:** M.W. has received research grants from Quercis and Versameb and honoraria for lectures or advisory board participation or consulting from Bayer, Curevac, Medac, Neurosense, Novartis, Novocure, Orbus, Philogen, Roche, and Servier. T.W. has received honoraria from Philogen. T.P.R. and M.K. hold equity in Cellis. M. Bialasek, B.T., I.M., T.P.R., and M.K. are inventors of intellectual property related to this work [patent application numbers: PCT/EP2016/064484 (Cellular targeted active ingredient delivery system), PCT/ EP2016/064483 (Cellular targeted active ingredient delivery system), PCT/PL2016/050057 (Cellular targeted pharmaceutically active substance or label delivery system), PCT/EP2021/056996 (Ferritin variants with increased stability, complexation ability and transferrin receptor affinity), PCT/EP2022/057205 (Ferritin variants with increased stability and complexation ability), and EP22195466.2 (Isolated targeted delivery system for the treatment of glioma)]. M. Bialasek, I.M., B.T., D.K., M. Siemińska, J.N., J.B., W.L., T.P.R., and M.K. are employees of Cellis. Cellis is a company pursuing the commercial development of this technology. There are no conflicts with this current research. All other authors declare that they have no competing interests. **Data and materials availability:** All data associated with this study are present in the paper or the Supplementary Materials. Ferritin and ferritin-drug conjugate are available from Cellis under a material transfer agreement with Cellis. The mass spectrometry proteomics data have been deposited to the ProteomeXchange Consortium by the PRIDE (*46*) partner repository with the dataset identifier PXD060767.

Submitted 1 July 2024
Resubmitted 18 December 2024
Accepted 28 May 2025
Published 18 June 2025
10.1126/scitranslmed.adr4058